Chapter 6

Exploration of the applicability of Low Temperature Nuclear Orientation (LTNO) to EB-systems and related systems

6.1 Introduction

The coupling in EB systems is strongly governed by the interactions at the FM/AFM interface. The introduction of a non-magnetic spacer between FM and AFM, such as Cu, Ag or Au, modifies the interfacial coupling. Therefore it is of great interest to get information on the spin directions in the vicinity of the interface and to study the effects of how induced magnetic moments are generated or transferred across a spacer layer. This is difficult to investigate by macroscopic methods. Microscopic methods, like LTNO, can give complementary information using e.g. Au probes in ultrathin Au spacer layers. In this work, the first measurement of the EB effect in the ferromagnetic layer and in the adjacent non-magnetic layer at the same time will be demonstrated using LTNO.

Besides FM/spacer/FM and FM/spacer/AFM EB systems, the remaining obvious combination of magnetic layers is the system AFM/spacer/AFM. While FM/spacer/FM systems were subject to many other studies, as can be found in the literature ([PMR90], [Bru95] and references therein), the experiments on thin AFM/spacer/AFM films have as yet rarely been addressed,

since there are not many techniques which are sensitive to probing the magnetic properties of this type of system containing intrinsic AFM layers. For most AFM materials with Néel temperatures near room temperature, such as e.g. CoO, the magnetic anisotropy is prohibitively high (over $\sim$ 20 T). Thus one will have difficulties investigating this system without a FM "sensor" layer, since most experimental techniques are sensitive only to macroscopic detection of the magnetization. The present results on CoO/Au/CoO are the first experiments probing the induced nuclear magnetization in a non-magnetic Au interface adjacent to an AFM layer via LTNO. The first demonstration of apparent coupling/interference effects between two AFM materials will be presented by observing the magnetic moments induced in the spacer layer as a function of its thickness. These results provide further information about the role of the AFM in an EB trilayer.

Hyperfine field techniques such as LTNO can measure the average nuclear spin polarization (alignment and magnitude of the magnetic hyperfine field) of both the magnetic (e.g. Co) and the non-magnetic spacer (e.g. Au) layer atoms at the same time. In contrast, conventional experimental techniques in magnetism, including SQUID magnetometry, vibrating sample magnetometry (VSM), Brillouin Light Scattering (BLS) and Ferromagnetic Resonance (FMR) are solely determined by the response of the magnetic layer atoms.

LTNO determines the average magnitude of the alignment of the nuclear magnetic moments $<I_z^2>$ (and also higher even orders) with respect to the applied magnetic field, by observing the anisotropic γ-ray emission from radioactive probe nuclei [SP86]. Using hyperfine field techniques, most investigations on magnetic layer systems containing thin non-magnetic spacers have shown that strong spin polarizations (hyperfine fields $\geq$ 3 T) in the spacer are restricted to the first layer at the interface to the magnetic material. This has been demonstrated experimentally using Perturbed Angular Correlations (PAC) measurements on Fe/Ag multilayers with ^{111}Cd probes [RDF+97], as well as by Mössbauer studies performed on Au/Ni and Au/Fe bilayers [KNES94]. Thus one expects LTNO to be sensitive to the non-magnetic spacer atoms adjacent to a magnetic layer.

LTNO is expected to be a suitable method to explore such layer systems which contain appropriate non-magnetic materials that provide long lived radioactive isotopes, such as ^{60}Co for Co and CoO and ^{198}Au for Au layers.

In this work, LTNO measurements on the Au and Co nuclear spin polarization in Co/Au/CoO EB systems, in Co/Au/Co and in CoO/Au/CoO systems with different Au layer thicknesses are presented. In order to measure the nuclear spin polarization, the γ-ray intensities from ^{60}Co in Co (CoO) and ^{198}Au in Au, emitted by a previously neutron irradiated sample, were detected

simultaneously.

The EB effect of the FM/Au/AFM trilayers across the non-magnetic Au spacer has been described previously in chapter 4, where an analysis of the magnetic properties for the Co/Au/CoO layer systems investigated, via SQUID magnetometry, was given. It was demonstrated that, even for larger spacer thicknesses of 2.25 nm, where the FM and AFM layers are completely separated, the coupling strength still amounts as much as 0.1 erg/cm^2. This supports the assumption that EB is not necessarily a (next-)nearest neighbor coupling mechanism [GGR01]. A detailed structural analysis of the present samples is given in chapter 3.

Using LTNO to investigate Co/Au/CoO trilayers, the γ-radiation emitted from the FM and AFM layers cannot be separated, since the radioactive probe isotope in the FM (Co) and the AFM (CoO) layer is in both cases ^{60}Co. However, the main contribution to the measured ^{60}Co γ-intensity from the EB systems is emitted from the FM layer, because the AFM layer is thin (2 nm) compared to the FM layer (16.4 nm): the AFM contains about 10% of the radioactive ^{60}Co atoms which are distributed in the Co and CoO layers of the EB-trilayer. However, in a Co/Au/CoO EB trilayer there are two Au interfaces, one neighboring the FM Co layer and the other one adjacent to the AFM CoO. Thus the γ-intensity resulting from the radioactive ^{198}Au probes which are situated in both Au interfaces will be averaged over the two types of sites and cannot be separated. The experiments on CoO/Au/CoO trilayers with two AFM/Au interfaces and on Co/Au/Co trilayers with two Co/Au interfaces provide the possibility to separately explore the two types of interfaces.

In the following sections the technique of LTNO, which is a hyperfine-field technique, will be introduced. In the first section, the contributions to the magnetic hyperfine fields will be described. The next section deals with the interaction of oriented (radioactive probe) nuclei with the hyperfine fields, resulting in an anisotropic γ-ray distribution. Additionally, a short description of the parameters determining the γ-ray distribution will be given. Subsequently the experimental setup is treated. Finally, the experimental results will be presented and discussed.

6.2   Some general aspects about hyperfine fields

The total magnetic hyperfine field experienced at a nuclear probe in a solid (e.g. at ^{60}Co atoms in Co) contains several different contributions and can be

expressed as follows:

$$\vec{B}_{total} = \vec{B}_{ext} + \vec{B}_{HF} + \vec{B}[\sum_{i=wholesample} dipoles)], \qquad (6.1)$$

where $\vec{B}_{ext}$ is the externally applied field and $\vec{B}_{HF}$ is the magnetic hyperfine field, which effectively probes the environment of the nucleus.

$\vec{B}[\sum_{i=wholesample} dipoles)]$ is due to the sum of all dipole-dipole interactions between the magnetic moments that make up the lattice. In some ideal cases the dipole term may be separated into a demagnetization field, caused by finite sample dimensions, and a sum of dipolar fields from the local environment of radius r, (Lorentz sphere), i.e. a sum of dipoles within this sphere and a Lorentz field (which is the demagnetization field of the sphere). However in thin magnetic films the last-mentioned contributions are of the order of less than 1 Tesla and may be neglected compared to the larger contributions to the hyperfine field. The magnetic hyperfine field at a nucleus is caused by the interaction between the nuclear magnetic moment and the magnetic field generated by the electrons at the site of the nucleus. The strength of the hyperfine field can be up to the order of magnitude of 400 Tesla. The hyperfine field of the local atomic probe environment B_{HF} can be separated into three terms [Sto86]:

$$\vec{B}_{HF} = \vec{B}_{L\ (Orbital)} + \vec{B}_{S\ (Dipolar\ S)} + \vec{B}_{FC\ (Fermi\ Contact)}. \qquad (6.2)$$

The three hyperfine contributions are illustrated in Fig. 6.1.

Interaction of the nuclei with non-s-electrons - the orbital contribution

The first term in the preceding equation is the contribution to the hyperfine field which arises from the interaction of the nuclear moment with the electron orbital motion. Each electron produces a field at the nucleus, which can be written as follows:

$$\vec{B}_{l_i} = \frac{\mu_0}{4\pi} \int \frac{\vec{r} \times \vec{v}}{r^3} dq = -\frac{\mu_0}{4\pi} \frac{l_i \hbar}{m_e} e \langle r_{l_i}^{-3} \rangle = -\frac{\mu_0}{4\pi} 2\mu_B \vec{l_i} \langle r_{l_i}^{-3} \rangle, \qquad (6.3)$$

where $\mu_B = \frac{\hbar e}{2m_e}$ is the Bohr magneton, μ_0 the permeability of vacuum and l_i the z-component of the orbital angular momentum of the i-th electron. The distance from the i-th electron to the center of the nucleus is given by the expectation value $\langle r_{l_i}^{-3} \rangle$.

Assuming weak spin-orbit coupling between the electron spins and their orbital moments, all the electrons of a single shell produce the following field:

$$\vec{B}_L = -\frac{\mu_0}{4\pi} 2\mu_B \vec{L} \langle r^{-3} \rangle \tag{6.4}$$

with $\vec{L} = \sum_i \vec{l}_i$ (Russel-Saunders coupling) and $\langle r^{-3} \rangle$ the average radial distance of the orbitals in the shell. The orbital contribution vanishes for s-shells, since all electrons have $l = 0$. It also vanishes for closed and half-filled subshells in free atoms. Very often the orbital contribution is much smaller than expected from the previous equations, because the electronic orbital angular momentum is quenched by the crystal field in a solid. In contrast, in the case of the rare earth metals with partially-filled f-shells, the orbital hyperfine field becomes the most important contribution since the spin-orbit coupling is stronger than crystal field effects.

Interaction of the nuclei with electronic spins - the dipolar contribution

The dipole moment of the electronic spin causes a magnetic field at the nucleus given by [Sto86]:

$$\vec{B}_{s_i} = -\frac{\mu_0}{4\pi}[\vec{\mu}_{s_i} - 3(\vec{\mu}_{s_i} \cdot \vec{r}_{u_i})\vec{r}_{u_i}] \langle r_i^{-3} \rangle, \tag{6.5}$$

where $\vec{\mu}_{s_i} = -2\mu_B \vec{s}_i$ is the magnetic moment of the electron and $\vec{r}_{u_i}$ a unit vector along $\vec{r}_i$. Assuming again Russel-Saunders coupling, the dipolar contribution of one electron shell is given by [Sto86]:

$$\vec{B}_S = -2\frac{\mu_0\mu_B}{4\pi}[\vec{S} + 3(\vec{S} \cdot \vec{r}_u)\vec{r}_u] \langle r^{-3} \rangle. \tag{6.6}$$

This interaction vanishes for spherically-symmetric spin density contributions and for materials with closed or half-closed subshells.

Interaction of the nuclei with s electronic spins - the Fermi contact interaction with core polarization and conduction electron polarization

The s electrons, which have a finite probability to be at the position of the nucleus, produce a magnetic field which is called the Fermi contact field. This field is the dominant contribution to the hyperfine field in many cases.

The magnetization M_0 produced by s electrons produces a field at an idealized point nucleus which is given by:

$$\vec{B}_{FC} = \frac{\mu_0}{4\pi} \cdot \frac{8\pi}{3} \vec{M}_0. \tag{6.7}$$

Since the magnetization density is induced by the s electron density at the nucleus, and assuming the electron wave function to be constant over the nuclear volume, the Fermi contact field is given by [Sto86]:

$$\vec{B}_{FC} = -\frac{\mu_0}{4\pi} \cdot \frac{8\pi}{3} g_S \mu_B \vec{S} |\psi_S(0)|^2 \tag{6.8}$$

where $|\psi_S(0)|^2 = \rho_0$ is the electron spin density at the nucleus.

Since electrons in the core states (spin up and spin down) are paired, the contribution 6.8 vanishes. However, experimentally it was found that large hyperfine fields can be observed even for s-state ions, e.g. for the Mn^{2+} ion ($3d^5, L = 0, S = \frac{5}{2}$) (see Ref. [Sto86] and references therein). In this case, the observed large hyperfine splittings can be attributed to the exchange and correlation interactions between the core s-state spins and the spins of the polarized $3d$ electrons. They cause a difference between spin-up and spin-down electron density at the nucleus and thus a magnetic hyperfine splitting through the Fermi contact term. The exchange interaction induces a net attraction between parallel spins and thus the s electrons of the inner closed shells are shifted with respect to the magnetic moment. In particular an inner s electron with its spin parallel to the magnetic moment is attracted by the outer electrons and shifted further away from its pair-electron-partner and from the nuclear center. Thus a net spin polarization at the site of the nucleus is produced, called core polarization. This is schematically illustrated in the bottom part of Fig. 6.1. The Fermi contact field is therefore proportional to the net spin density, given by the difference between the spin-up and the spin-down density at the site of the nucleus, as in the following equation [Sto86]:

$$\vec{B}_{CP} = \frac{8\pi}{3} g_S \mu_0 \mu_B \vec{S} \sum_{n,s} [|\psi_{ns}^\uparrow(0)|^2 - |\psi_{ns}^\downarrow(0)|^2]. \tag{6.9}$$

The core polarization contribution to the Fermi contact field is negative (with respect to the net magnetic moment), if the s subshell considered lies predominantly within the unpaired electron subshell on which the net spin resides (see also illustration in Fig. 6.1); and positive, if it is outside that subshell.

Interaction Hamiltonian $\mathscr{H}$:

$$\mathscr{H} = \mathbf{B} \bullet \quad = - \quad_N g \, \mathbf{B} \bullet \mathbf{I}$$

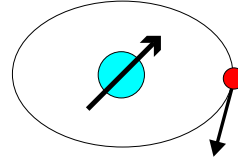$$\mathbf{B} = \mathbf{B}_{ext} + \mathbf{B}_{\{dipoles\}} + \mathbf{B}_{HF}$$

The Hyperfine Interaction:

$$\mathbf{B}_{HF} = \mathbf{B}_L + \mathbf{B}_S + \mathbf{B}_{FC}$$

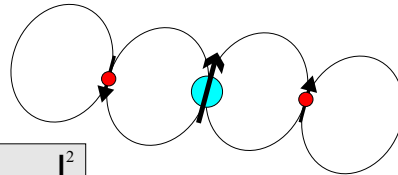**Interaction of nucleus with non-s electrons :**

$$\mathbf{B}_{L(Orbital)} = \quad 2(\quad_0/4 \quad \quad \mathbf{L} <r^{-3}>$$

Interaction of nucleus with the sum of dipoles "outside" the nucleus :

$$\mathbf{B}_{S(Dipolar\,S)} = \quad 2(\quad_0 \quad /4 \quad [\mathbf{S} - 3(\mathbf{S}*\mathbf{r_u})\mathbf{r_u}] <r^{-3}>$$

Fermi-Contact term :

$$\mathbf{B}_{FC\,(Fermic\,Contact)} = (\quad_0/4 \quad 8 \quad * \quad g_S * \mathbf{S} * | \quad |^2$$

Fermi-Contact - Core Polarization:

$$\mathbf{B}_{CP} = (8 \quad *g_S \quad_0 \quad *\mathbf{S}*_{n,s} [\,|\quad^{\uparrow}_{ns}\quad|^2 - |\quad^{\downarrow}_{ns}\quad|^2\,]$$

s-electrons usually have part of their wave function overlapping the nucleus, i.e.$|$ (0) (0)*$|$ is non-zero. There are two contributions:

   a) Core s-electrons (e.g. 1s, 2s and 3s)
   b) Valence or conduction s-electrons with
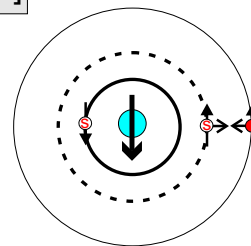   Bloch-like wavefunctions   u($\mathbf{r}$)e^{ikr}

Figure 6.1: Hamiltonian and hyperfine interaction for the nuclear probe. The terms describing the different hyperfine field contributions are given for the case of simple LS-coupling.

The core polarization term is important, if not dominant, for all systems with non-zero resultant spin. For $3d$ elements, the values of B_{CP} are approximately proportional to the number of unpaired electrons, i.e. to the magnetic moment.

Another source of non-zero spin density at the site of the nucleus is the polarization of s-like conduction electrons arising from the magnetic moment of the atomic neighbors or an external field. These polarized conduction electrons again cause a non-zero net spin density between spin-up and spin-down at the nucleus which contributes to the Fermi contact field. In total, a phenomenological formula for the Fermi contact field in a ferromagnet can be given as [Sto86]:

$$\vec{B}_{FC} = a\vec{\mu} + \sum_i a_i \vec{\mu}_i(r_i). \qquad (6.10)$$

In the first term, $\vec{\mu}$ represents a local magnetic moment which causes a hyperfine field at the site of the nucleus, as described before (core polarization contribution). The parameter a is the local moment coupling parameter. The second term in Eq. 6.10 summarizes the contributions due to the polarization effects caused by the conduction electrons of the neighboring atoms (conduction electron polarization contribution) with their moments $\vec{\mu}_i$. The a_i then describe the strength of the influence of the atomic neighbors.

In the present work, Co/Au/CoO and related systems are investigated. Therefore, at the end of this section a table (Tab. 6.1) is given where calculated values for the the different hyperfine field contributions for Co in Co metal [RGPyB+02] (calc.), [ZHEE78] (exp.) and Co in CoO [Mot60] (calc.), [OY77] (exp. and calc.) are listed as concrete examples.

The hyperfine fields experienced by Au are mainly caused by conduction electrons that are polarized through the magnetic moments of the next-nearest neighbor Co atoms, and it is to be expected that the direction of the Au hyperfine field is the same or opposite to that of the Co hyperfine field.

6.3 The LTNO method

6.3.1 Interaction of the nuclear moments with the hyperfine field

All nuclei with a non-zero spin have a magnetic dipole moment which interacts with the magnetic field acting on the nucleus. This field is comprised of different field contributions as described in detail in Eq. 6.1 and the following equations. In the case of the layer systems investigated, (Co/Au/CoO) and

system Co in	B_L in T	B_S in T	B_{CP} in T	B_{VP} in T	B_{HF} in T	exp. in T
Co	5.9	-0.059	-19.39	-7.12	-20.68 [RGPyB$^+$02]	-21.87(5) (hcp) [ZHEE78] -21.63(5) (fcc) [ZHEE78]
CoO	72.1	2.77	-26.4	-	48.5 [OY77]	49.5(5) [OY77]

Table 6.1: *Different contributions to the magnetic hyperfine field B_{HF} which acts on a nucleus: the orbital contribution B_L; the dipolar contribution B_S; the core polarization contribution (Fermi contact) B_{CP}; the contribution B_{VP} (Fermi contact)due to the polarization of the conduction electrons caused by next nearest neighbor moments.*

(CoO/Au/CoO) and (Co/Au/Co), the hyperfine field B_{HF} is the most important field contribution for nuclear orientation. In particular, for Co in FM Co metal, the core polarization contribution dominates, whereas in CoO the orbital hyperfine contribution dominates [OY77]. The interaction Hamiltonian between the nuclear dipole and the magnetic field is:

$$H = -\vec{\mu}_I \cdot \vec{B}_{total} \tag{6.11}$$

with $\vec{\mu}_I = g\mu_N \cdot \vec{I}$ ($\vec{I} = I\vec{e}$; $\vec{e}$ *is a unit vector in the direction of the nuclear spin*), where $\mu_N = \frac{e\hbar}{2m_p} = 5.05 \times 10^{-27}$ Am^2 is the nuclear magneton with m_p the proton mass. The gyromagnetic ratio of nuclei with spin I is expressed by the dimensionless factor $g = g(I)$ (see also Ref. [SW92]). The nuclear angular momentum $\vec{I} = \vec{L}_N + \vec{S}_N$ is composed of a nuclear orbital component and a nuclear spin component.

Under the influence of the magnetic field B_{total} a nuclear spin precession is induced, the degeneracy of the energy level with nuclear spin I is lifted and the level is split into equidistant sublevels with energies

$$E_m = -\mu_N g B_{total} m \tag{6.12}$$

with the quantum numbers $m = [I, I-1, ..., -I]$ and the z-direction defined along $\vec{B}$.

In addition to the magnetic dipole hyperfine interaction there is also an electric quadrupole interaction. It is caused by electrostatic interactions between nuclear quadrupole moments and electric field gradients (EFG) at the

site of the nuclei. Nuclei with spins $>1/2$ have an electric quadrupole moment eQ. That moment interacts with an EFG $eq = \frac{\delta^2 V}{\delta z^2}$ existing at the site of the nucleus. The EFG is caused by potential (V) differences in the electronic environment of a nucleus, which produces an energy shift of the nuclear sublevels. However, the energy shifts to the nuclear sublevels are generally small compared to the induced hyperfine field (not always true for rare earths) and can be neglected for the purposes of this work.

6.3.2 γ-radiation emitted by oriented nuclei

Quantum levels of nuclei are characterized by a well-defined total angular momentum I and parity π. In the transition from a higher to a lower energy level often γ-rays are emitted. The following conservation laws have to be fulfilled for the transition:

$$
\begin{aligned}
energy: \ E_i &= E_f + \hbar\omega \\
angular\ momentum: \ \vec{I_i} &= \vec{I_f} + \vec{l} \\
parity: \ \pi_i &= \pi_f \pi.
\end{aligned}
\tag{6.13}
$$

During the transition from the initial state $(I_i, \ M_i, \pi_i)$ to the final state $(I_f, \ M_f, \pi_f)$, a photon with the quantum numbers $(l, \ m, \ \pi)$ is emitted. The emission of a photon is equivalent to the creation of an electromagnetic wave with energy $\hbar\omega$. The conservation of angular momentum and parity requires that the emitted wave, like the nuclear states, have a well-defined angular momentum and parity [SW92].

When the ensemble of nuclei is in thermal equilibrium the population of the nuclear quantum levels a_m is given by:

$$
a_m = \frac{exp(-\frac{E_m}{kT})}{\sum_m exp(-\frac{E_m}{kT})} \ .
\tag{6.14}
$$

Orientation of a nuclear ensemble means that the populations of the nuclear sublevels are different. Here two cases have to be distinguished:

1) pure alignment of the nuclei with $a_m = a_{-m}$ for all m and

2) polarization of the nuclei with $a_m \neq a_{-m}$.

In the case of γ-ray emission from an oriented nucleus, the emission angle Θ of a particular γ-ray depends on the scalar product of its wave vector and the nuclear spin: $\mathbf{k}_\gamma \cdot \mathbf{I}$. This product is a pseudo-scalar, which changes sign under space inversion because $\mathbf{k}_\gamma$ changes sign, while $\mathbf{I}$ does not. Since the basic laws of electromagnetism are invariant under this operation, the γ-ray directional distribution function should also be invariant and thus the latter

may depend only on even powers of $cos\Theta$. Hence only even orders of $< I_z^\mu >$ (i.e. $\mu = 2, 4, ..$) occur in the directional distribution function.

Because of the symmetry of γ decay, the γ-rays thus have an equal probability of being emitted in the $+z-$ or $-z$-directions, hence the measurement of γ-rays is sensitive only to the degree of nuclear alignment. With a Boltzmann distribution for a nuclear spin larger than $1/2$ and magnetic interactions, one has both nuclear polarization and alignment.

Radiation from oriented nuclei is emitted isotropically if the thermal energy is much larger than the energy difference between nuclear sublevels (i.e. $T > 1$ K). Then the sublevel populations will be nearly equal and no orientation can be observed (see Fig. 6.2).

To achieve measurable nuclear orientation, the energy difference between nuclear sublevels ΔE_m should be of the same order of magnitude as the thermal energy kT. This leads to the following condition:

$$\frac{\mu_n g B_{total} \Delta m}{k} \approx T. \tag{6.15}$$

Assuming for example $\Delta m = 1$, this condition requires a B/T ratio of the order $10^3 \ T/K$ or more to achieve sizable differences between nuclear sublevel populations. Currently, temperatures around 5 mK are achievable with a $^3He/^4He$ dilution cryostat [BC86], [SW92]. The working principle of such a cryostat is explained in section 6.4 and illustrated in Fig. 6.3. The required high fields are provided by superconducting magnets or by making use of the often strong magnetic hyperfine fields present in many materials. The directional distribution of γ-rays which are emitted by an axially symmetric nuclear ensemble, the γ anisotropy $W(\Theta)$, can be calculated from the solutions to the Maxwell equations in the form of multipole radiation. One possible description of the γ-ray anisotropy is given by the following equation [SP86]:

$$W(\theta_{Di}) = 1 + \sum_{k=2,4} B_k U_k A_k Q_k P_k(\cos \Theta_{Di}). \tag{6.16}$$

As explained above, γ-radiation is sensitive only to the alignment of nuclei. Therefore only the even terms of the expansion 6.16, given above will contribute to the anisotropy. The γ anisotropy is the product of

- the orientation parameters B_k (definition of B_k: see Ref. [BSG57]), which are functions of the hyperfine interaction and the temperature;

- the angle dependent Legendre Polynomials, where Θ_{Di} is the angle between the detector D_i axis and the quantization axis;

- the nuclear deorientation parameters U_k, which are coefficients describing deorientation effects caused by unobserved transitions (e.g. through intermediate states),

- while the A_k coefficients depend only on the parameters of the observed γ-transition;

- the Q_k are solid-angle corrections arising from the detector-source geometry, which defines a finite solid angle. These parameters approach 1 for infinitely small solid angles (ideal point-like detector).

In the following, these parameters are briefly described (on the basis of Ref. [Kra86]):

The orientation parameters B_k

The orientation parameters B_k are functions of the hyperfine interaction and the temperature. Using the definition of Blin-Stoyle and Grace (Ref. [BSG57]), they are given by the following relation (for the case of an axially symmetric system):

$$B_k(I) = \sqrt{2k+1} \ \sqrt{2I+1} \ \frac{\sum_m (-1)^{I+m} \begin{pmatrix} I & I & k \\ -m & m & 0 \end{pmatrix} exp(m\Delta_m/T)}{\sum_m exp(m\Delta_m/T)}. \quad (6.17)$$

From the properties of the Wigner 3j-symbols (see appendix), it follows that, when $k > 2I$, the B_k parameters vanish. In the case of pure alignment, the orientation parameters with k odd are zero. The number of the terms in Eq. 6.17 is limited by the spin of the oriented state. A table with the B_k parameters as a function of I and $\Delta_m = \frac{\mu_I B_{total}}{kI}$ can be found in Ref. [Kra86]. The nuclear orientation is basically a function of the population of the nuclear sublevels (which is temperature dependent). To elucidate the relation between the B_k orientation parameters and the populations a_m (given by Eq. 6.14), for the case of B_2, the following equation is given [SP86]:

$$\sum_m (\frac{I_z}{I})^2 a_m - \frac{1}{3}\frac{(I+1)}{I} = const. \cdot B_2(I). \quad (6.18)$$

Thus B_2 depends mainly on the population a_m and on $(I_z)^2$. The second-order term B_2 will prove to be the strongest contribution to the nuclear orientation for the present experiments; for the case of ^{198}Au 4th order effects can be neglected, while for ^{60}Co they become important only at low temperatures. Our measurements basically are sensitive to $(I_z)^2$.

The Legendre Polynomials P_k

The angular dependence of the γ anisotropy $W(\Theta)$ is given by the Legendre Polynomials $P_k(cos\Theta)$ where Θ is the angle between the applied field axis and the quantization axis of the nuclear moments. In the case of the present system, this is the angle between the detector and the direction of the average hyperfine field at the ^{60}Co and ^{198}Au nuclei.

The deorientation parameters U_k

The oriented state of the layer systems investigated here, containing Au and Co and CoO layers, is the $I = 2$ state in the case of ^{198}Au and the $I = 5$ state in the case of ^{60}Co. The observed γ-rays are the 412 keV line following the ^{198}Au β-decay, and the 1173 keV and 1332 keV lines following the ^{60}Co β-decay, respectively. They are emitted from states which are reached after β-decay of the oriented $I = 2$ (Au) and $I = 5$ (Co) states. These states can be followed by several unobserved intermediate transitions, which tend to equalize the populations a_m; therefore the orientation of the levels observed is less than the initial-state orientation. The deorientation parameters U_k are given by [Kra86]:

$$U_k(I_i, I_f, L) = (-1)^{I_i+I_f+L+k}\sqrt{2I_i + 1} \ \sqrt{2I_f + 1} \ \begin{Bmatrix} I_i & I_i & k \\ I_f & I_f & L \end{Bmatrix}, \quad (6.19)$$

where I_i and I_f are the nuclear spins of the initial and final states and L is the multipole order of the intermediate γ-ray transition (for the $6j$-symbol see appendix). In the case where the connection between the initial and final states is a cascade through different levels, a product of all deorientation parameters leads to the total deorientation coefficient. If there are several different branches which connect the initial and final state, the total deorientation coefficient is the weighted sum of the contributions belonging to the different γ-ray transitions with their corresponding intensities:

$$U_k(I, I_1, ...I_j) = \sum_n w_n[U_k]_n. \quad (6.20)$$

The angular distribution parameters A_k

The radiation is emitted anisotropically because of the vector coupling between the initial and final spins and the angular momentum $\vec{l}$ of the emitted γ-ray:

$$\vec{I_1} = \vec{I_2} + \vec{l}. \quad (6.21)$$

If the initial state is oriented, the final state and the angular momentum will be spatially oriented as well (conservation of angular momentum). The angular distribution parameters for γ-rays with a maximum of two multipolarities l and $l' = l + 1$ are given by the following equation [Kra86]:

$$A_k = \frac{F_k(llI_2I_1) + 2\delta F_k(ll'I_2I_1) + \delta^2 F_k(l'l'I_2I_1)}{1 + \delta^2}, \qquad (6.22)$$

where δ is the mixing ratio of the two multipole orders and the coefficients F_k are given by:

$$F_k(ll'I_2I_1) = (-1)^{I_1+I_2+1}\sqrt{2k+1} \ \sqrt{2l+1} \ \sqrt{2l'+1} \ \sqrt{2I_1+1}$$
$$\times \begin{pmatrix} l & l' & k \\ 1 & -1 & 0 \end{pmatrix} \begin{Bmatrix} l & l' & k \\ I_1 & I_1 & I_2 \end{Bmatrix}. \qquad (6.23)$$

The angular distribution parameters for γ-rays are zero when k is odd, which means that γ-radiation is sensitive only to alignment (and not to polarization).

It is the angular distribution parameters A_k which account for the symmetry of the γ-decay (directional distribution is a function only of the even powers of the scalar product $\mathbf{k}_\gamma \cdot \mathbf{I}$), and cause all contributions to the anisotropy $W(\Theta)$ given in Eq. 6.16 with k odd to vanish, because all A_{odd} vanish.

The 1173 keV and the 1332 keV lines from ^{60}Co, as well as the 412 keV line from ^{198}Au, are pure $E2$ transitions (notation from electrical 2^l pole $= El$ radiation with the quantum number $l = 2$ in the cases considered). From the properties of the 3j-symbols, it follows that only terms with $k \leq 2l$ are nonzero. For the previously considered transitions, this means, that only $k = 2$ and $k = 4$ terms have to be taken into account in Eq. 6.16. If the 4th order contribution is small compared to the 2nd order contribution, it can be neglected. Because of the properties of the 2nd order Legendre polynomial P_2, $|W(0) - 1|$ should then be almost twice as large as $|W(90) - 1|$, if the Q_k coefficients are almost equal (which is often the case). The shape of this γ radiation distribution, projected into the sample plane, is illustrated in Fig. 6.2.

The solid angle correction factors Q_k (detector geometry)

In the case of γ radiation, the Q_k are geometrical correction factors taking into account the finite size of the sample and the detector. These coefficients depend on the detector geometry and efficiency, the distance between the source and the detector and the energy of the γ-rays and they can be calculated.

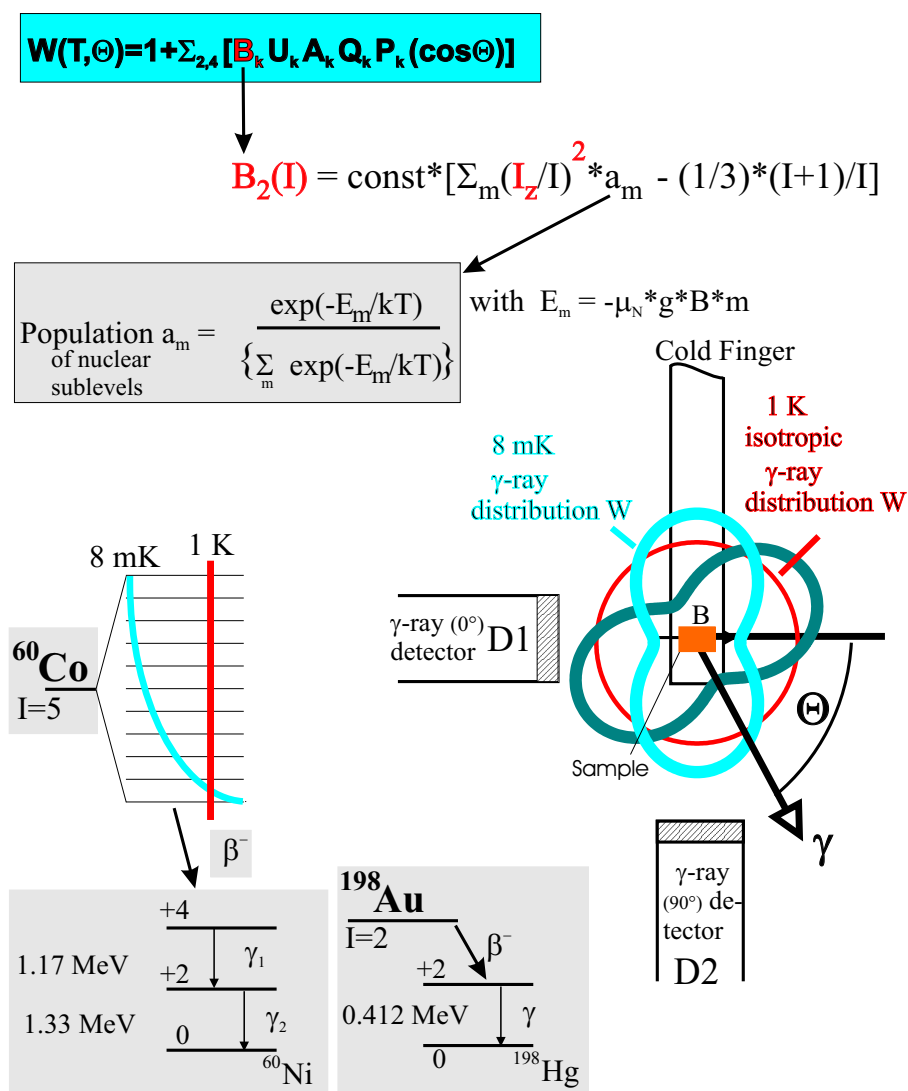The working principle of a LTNO experiment is illustrated in Fig. 6.2.

$$W(T,\Theta) = 1 + \Sigma_{2,4}\,[B_k\,U_k\,A_k\,Q_k\,P_k(\cos\Theta)]$$

$$B_2(I) = const * [\Sigma_m (I_z/I)^2 * a_m - (1/3)*(I+1)/I]$$

$$\text{Population } a_m = \frac{\exp(-E_m/kT)}{\{\Sigma_m \exp(-E_m/kT)\}} \quad \text{with } E_m = -\mu_N * g * B * m$$
of nuclear sublevels

Cold Finger

1 K isotropic γ-ray distribution W

8 mK γ-ray distribution W

8 mK   1 K

^{60}Co
I=5

γ-ray (0°) detector D1

B

Sample

Θ

γ

β⁻

+4

1.17 MeV   +2   γ₁

1.33 MeV   0   γ₂

^{60}Ni

^{198}Au
I=2   β⁻

+2

0.412 MeV   γ

0   ^{198}Hg

γ-ray (90°) detector

D2

Figure 6.2: Working principle of an LTNO experiment. The radioactive probe isotopes ^{198}Au and ^{60}Co are produced by irradiation of the samples containing natural ^{197}Au and ^{59}Co with thermal neutrons in the nuclear reactions described by ^{197}Au+n–>^{198}Au (2.7 d) and ^{59}Co+n–>^{60}Co (5.27 y).

6.3.3 Thermometry via oriented nuclei

In order to determine the orientation parameters B_k, the temperature of a sample has to be known. The normal way to determine the temperature is to use a calibrated radioactive sample with well known parameters, which is soldered onto a cold-finger (thermally connected to the sample holder) as close as possible to the sample. In the present case, a ^{54}Mn in Ag thermometer was used (and for the last experiment a ^{54}Mn in Au thermometer).

Preparing such a thermometer requires a small quantity of ^{54}Mn, which is diffused in a Ag or Au foil. With diffused atoms, it is not certain that all radioactive nuclei are in substitutional sites in the Ag host lattice. This can be taken into account by introducing a substitutional fraction f in Eq. 6.16:

$$W(\theta_{Di}) = 1 + f \times \sum_k B_k U_k A_k Q_k P_k(\cos\Theta_{Di}) \ . \qquad (6.24)$$

Our thermometers were calibrated with a neutron-activated ^{60}Co in Co thermometer with a fraction $f = 1$. The fraction found for the ^{54}Mn in Au thermometer was $f = 0.797$; for the ^{54}Mn in Ag it was nearly 1. The decay of the ^{54}Mn isotope has one main γ-ray transition with an energy of 835 keV.

6.4 Experimental setup

6.4.1 Cooling by ^{3}He/^{4}He dilution refrigeration

The cooling principle of the ^{3}He/^{4}He dilution refrigerator, which is commercially available, used to reach mK temperatures ([BC86], [SW92]), is based on the fact that ^{3}He and ^{4}He are partly immiscible below 0.87 K. ^{3}He atoms are fermions and ^{4}He atoms are bosons, which does not play a role at higher temperatures, but below the coexistence curve, shown in Fig. 6.4, ^{3}He and ^{4}He separate spontaneously into two phases: a ^{4}He rich phase, which contains at most 6.4 % (below 100 mK) of ^{3}He, and a phase with mainly pure ^{3}He which floats on top because of its lower density. It is important that ^{3}He is soluble in ^{4}He to a certain extent even at the lowest temperatures. Thus the system tries to maintain the equilibrium state at a given temperature. If the concentration of ^{3}He in the ^{4}He rich phase passes over the critical value of 6.4 % (below 100 mK), the surplus condenses into the concentrated ^{3}He phase and heat is released, which is absorbed by the surroundings.

On the other hand, ^{3}He can be removed from the mixture by pumping on the ^{4}He-rich phase. To maintain the equilibrium concentration of 6.4 %, concentrated ^{3}He evaporates into the ^{4}He-rich phase and heat is taken up. Crossing this phase boundary is equivalent to increasing the entropy and thus
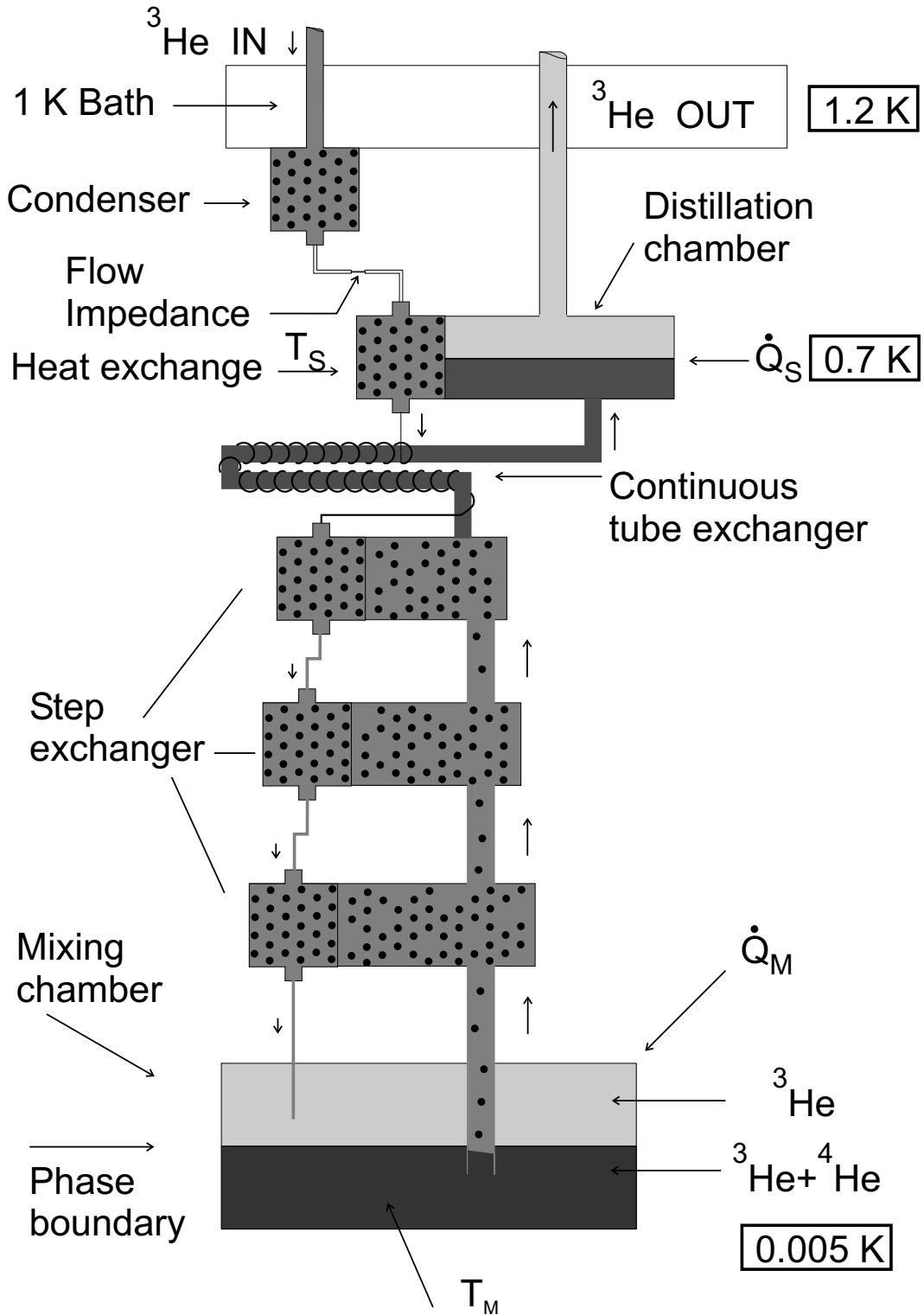
^{3}He IN ↓

1 K Bath →

^{3}He OUT   1.2 K

Condenser →

Distillation chamber

Flow Impedance

Heat exchange T_S →   ← $\dot{Q}_S$ 0.7 K

Continuous tube exchanger

Step exchanger

Mixing chamber

$\dot{Q}_M$

^{3}He

^{3}He+^{4}He

Phase boundary

0.005 K

T_M

Figure 6.3: Principal parts of a ^{3}He-^{4}He dilution refrigerator.
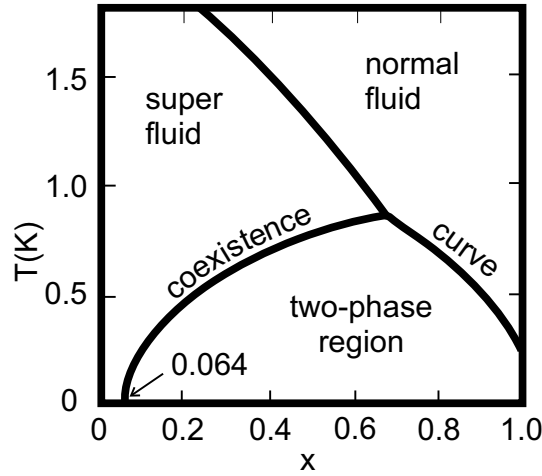
Figure 6.4: Phase diagram of a ^{3}He/^{4}He mixture. $x = \frac{n(^3He)}{[n(^3He) + n(^4He)]}$ is the ^3He concentration. The tricritical point is at 0.84 K (from [SW92]).

absorption of heat, resulting in cooling of the mixture. To maintain mK temperatures for some time, ^{3}He has to be continuously circulated. The ^{3}He (precooled by the 4K bath) coming from the condenser side is first condensed by thermal contact with the 1 K bath (see Fig. 6.3). The 1 K bath is a ^{4}He bath which is pumped to a temperature of approximately 1.1 K (evaporation cooling). Subsequently the circulating ^{3}He is further cooled to mK temperatures by a series of efficient heat exchangers, before it enters the mixing chamber (^{3}He rich side). ^{3}He is removed from the ^{3}He/^{4}He mixture by pumping on the distillation chamber. In the distillation chamber, the mixture is heated to about 0.7 K. At this temperature one makes use of the different equilibrium evaporation pressures of ^{3}He and ^{4}He. The evaporation pressure of ^{4}He at this temperature is much smaller than that of ^{3}He. Thus ^{3}He enters the gas phase and is separated from the ^{4}He by pumping (fractional distillation). The ^{3}He moves to the distillation chamber from the mixing chamber through osmotic pressure. The lowest temperatures achievable by this process are approximately 2 mK.

6.4.2 Experimental procedure

All samples were neutron activated for three days using a thermal neutron flux of $10^{13} \frac{n}{cm^2 s}$ at the BER-II research reactor of the Hahn-Meitner-Institut, Berlin. For neutron activation, they where sealed in a glass tube in an argon gas atmosphere. The argon gas ensures thermal contact to the cooling water

($50°C$) during the irradiation process and provides an inert atmosphere for the sample. During this process, the radioactive isotopes ^{198}Au (2.7 days) and ^{60}Co (5.27 years) are produced from the corresponding stable isotopes in the samples (see also Fig. 6.2). No significant radiation damage due to *gamma*-recoil or temperature rise is to be expected. Fast neutrons at the irradiation site were avoided by using a site outside the reactor core.

After activation, the radioactive samples were soldered onto a silver sample holder (cold finger) using a Ga-2% Sn eutectic. A ^{54}MnAg nuclear thermometer was soldered with Wood's metal onto the back side of the cold finger, as close as possible to the sample position. Wood's metal has a melting point of approximately 80°C. However, in wetting of both surfaces (the surface of the cold finger and that of the thermometer) usually requires higher temperatures of about 130°C. Heating the nuclear thermometer ^{54}Mn in Ag to this temperature causes no damage. Heating a multilayer to this temperature, on the other hand, might change its structure due to annealing. Therefore the Ga-Sn eutectic was used. It has a melting point between 20°C and 30°C, depending on the exact ratio of Ga and Sn. The magnetic field necessary to keep the solder normally conducting at 5 mK is about 2 mT [Pob96]. Thus the sample, the cold finger and the solder have to be warmed up to about 30°C to wet the surfaces during sample attachment. However it is not always the case that one is able to keep both surfaces wetted while the solder solidifies, which results in a poor thermal contact. This causes a low signal-to-noise ratio during an LTNO experiment. The samples which were used for LTNO experiments were prepared with 50 nm (and 100 nm respectively) thick Ag capping layers to provide thermal contact. But it should be mentioned that Ga tends to alloy with Ag, as well as with Au. Therefore at least the Au layer in a simple Co/Au bilayer with a Ag capping layer may be modified by the Ga penetrating the Ag and subsequently the Au. In this case it can also affect the Co at the interface and its properties might change. Therefore only measurements on Co/Au/Co with thick Ag capping layers are presented here, where the interfaces are not likely to be affected. If the interfaces were contaminated with Ga, the hyperfine-field values were strongly reduced. This was not seen in the experiments. The other magnetic systems investigated, such as as Co/Au/CoO/Ag and CoO/Au/CoO/Ag, seem to be well protected by the thin CoO layer, which is an insulator. The characteristic features of these EB systems have proved to be conserved, as can be seen from the results.

Before the samples were inserted into the $^3He/^4He$ cryostat, they were subjected to an applied field of > 400 mT to align the magnetic moments and to induce the EB effect. Subsequently they were top-loaded, together with a calibrated ^{54}Mn in Ag thermometer, into the cryostat and cooled to 4.2 K. At this temperature, a magnetic field of 500 mT was applied, followed

by cooling of the cold finger to the cryostat base temperature of < 5 mK. Unfortunately, the samples could not be continuously field-cooled from above the Néel temperature to the base temperature. In the case of the EB samples, the EB is retained (with some reduction) due to the remanence of about 80 % (see also Ref. [MGB$^+$99]).

The distribution of the γ-rays following the β-decays of both ^{198}Au and ^{60}Co can be expressed as given in Eq. 6.16.

The γ-ray intensity was monitored with two Ge detectors: Detector D1 (0° detector) was mounted parallel to the plane of the trilayers and along the applied field direction, and detector D2 (90° detector) was also mounted parallel to the sample plane but perpendicular to D1 (see Fig. 6.2).

The detector signals are amplified and sent to the computer, which controls the data recording. The computer is equipped with a Multi-Channel-Analyzer (MCA) realized by a (commercially available) TMCA card which allows one to record energy-resolved spectra. Therefore the detector signals are sorted into 1024 channels, i.e. each γ-ray with a particular energy is counted in a corresponding channel. The intensities are summed over a fixed time interval determined by the user. A typical energy spectrum of the EB samples is given in Fig. 6.5. From the energy spectrum, it is obvious that the intensity of the ^{198}Au γ-rays is much higher than that of the ^{60}Co γ-rays. The γ-ray intensity depends on various factors, such as the amount of material, the neutron capture cross section and the radioactive half-life. In the present case, there are 0.5 nm Au as opposed to 16.4 nm Co and 2 nm CoO, i.e. there is much more Co than Au to be irradiated. The neutron capture cross sections σ_c amount to 37 barn for ^{59}Co and 98.8 barn for ^{198}Au, i.e. according to the the cross section alone, the relative concentration of radioactive probe isotopes in the Au is higher than in Co. But finally it is the half life which mainly determines the relative intensity of γ radiation from ^{198}Au (2.7 days) and ^{60}Co (5.27 years). Thus, about three days after recording the spectrum shown in Fig. 6.5, the intensity of the ^{198}Au γ-rays is halved, while the ^{60}Co γ-ray intensity has hardly changed at all.

Each energy spectrum is saved in a file for further data processing. An appropriate data-processing tool allows one to select Regions of Interest (ROIs) around the important peaks, i.e. only the energy channel of maximum intensity of the important γ-rays and the neighboring channels are considered for further data processing. The software employed further provides a tool to integrate over the intensities and to subtract the background intensity within the boundaries of the ROI. In this way a large number of files (energy spectra) can be processed within a short time. The peak integration values attached to the corresponding γ-rays are saved in a new file, which is used for further data processing. Furthermore, the γ-ray intensities have to be corrected for
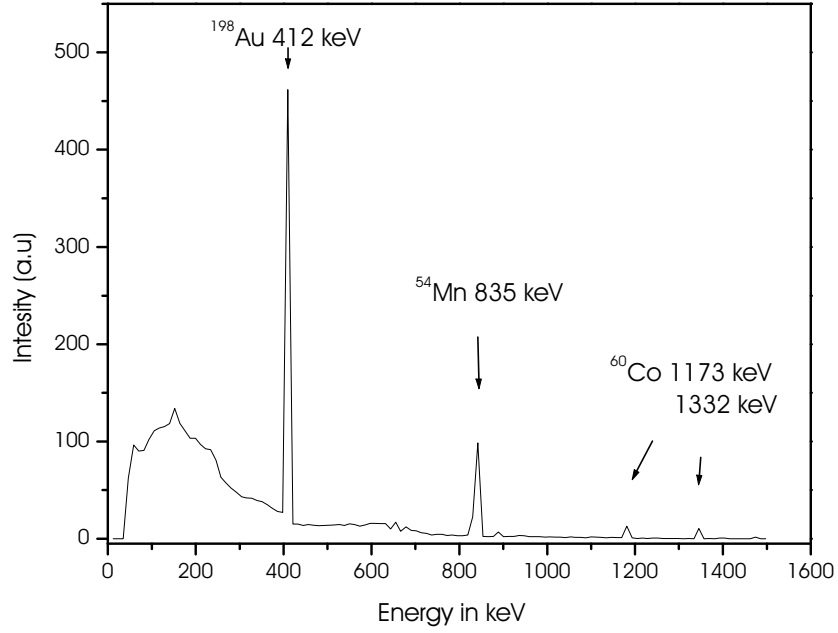
Figure 6.5: Typical energy spectrum from a Co/Au/CoO sample containing the radioactive isotopes ^{60}Co and ^{198}Au together with the ^{54}Mn in Ag thermometer.

their half-lives. Thereafter the intensities measured at mK temperatures (cold counts: anisotropic γ-ray distribution) were normalized to the γ-ray intensity measured at 1 K (warm counts: isotropic γ-ray distribution), yielding the magnitude $W(\Theta)$ which is a function of different parameters as can be seen from Eq. 6.16 (see also Fig. 6.2):

$$W(detector\ i) = \frac{I_{cold}}{I_{warm}}. \tag{6.25}$$

Finally after peak integration, background subtraction and life-time correction, the normalized γ-ray distribution $W(\Theta)$ can be plotted as a function of time, temperature or magnetic field.

At first, the initial cool-down curve is recorded, i.e. the γ-ray intensities are monitored during the cooling of the cryostat. In the present case, a constant field of 500 mT was applied during the cool-down. After processing the measured data as described above, the normalized γ-ray distribution $W(\Theta)$ was plotted as a function of time. At the base temperature of the cryostat, in addition a hysteresis curve was observed for each sample by measuring the γ-ray intensity with each detector as a function of sign and magnitude of the applied field.

Fig. 6.6 (center and bottom, right) schematically illustrates possible γ-ray distributions at mK temperatures (anisotropic) and at 1 K (isotropic). They are monitored by two detectors at fixed positions. From the ratio of the intensity deviations from W(Θ)=1, as measured by the two detectors at mK temperatures, the average angle Θ between the axis of the nuclear alignment and the applied field axis is obtained. Three energy spectra are given at the top of Fig. 6.6, such as would be measured by the detectors D1 and D2 at 5 mK (fine black line and red solid line) and at 1 K (solid line). The normalized γ-ray intensities W(Θ), which could be obtained from the detectors D1 (circles) and D2 (triangles), are schematically illustrated (center and bottom,left). The curves represent typical cool-down curves for both detectors corresponding to the γ-ray distributions for two different axis of nuclear alignment given on the right-hand side.

Data analysis

From the measured γ-ray intensities, the average magnetic hyperfine fields and the average angle between the hyperfine field and the detector can be extracted as indicated above. The hyperfine field at ^{60}Co in Co metal can be determined assuming that all ^{60}Co nuclei experience the same (average) hyperfine field. But there are two possibilities to determine the hyperfine field of ^{198}Au in a non-magnetic Au spacer: the first follows the assumption that all nuclei in the Au spacer experience the *same* average hyperfine field ("one site model"), while the second approach makes the assumption that only the Au nuclei situated at an interface with Co or CoO are subject to a large hyperfine field. The spacer layers further from the interfaces, on the other hand, are subject to a hyperfine field which is negligible, since the LNTO technique is not sensitive to hyperfine fields $< 3\ T$ ("two site model"). The calculation of this latter model is carried out by using a fraction f in Eq. 6.16 as also done in Eq. 6.24, where $1 - f$ is the fraction of ^{198}Au nuclei experiencing a negligible hyperfine field. The second approach was experimentally confirmed by [RDF$^+$97] performing PAC (Perturbed Angular Correlation) experiments on a Fe/Ag interface and by [KNES94] with Mössbauer spectroscopy on a Fe/Au multilayer. It was found in these experiments that only the Au and Ag nuclei adjacent to the ferromagnetic material experience large hyperfine fields. Additionally, first principle calculations with WIEN97 on Fe/Ag multilayers ([PPB$^+$01]) as well as on Co/Au and CoO/Au layers ([Pra02]) confirm these experimental results. The angle between the hyperfine field and the detector axis can be determined at the same time by using two detectors.

The hyperfine field of the ^{198}Au in the present work will be calculated using both procedures. The assumption of an average hyperfine field will be compared to the case where large hyperfine fields are restricted to the interface atomic layers.
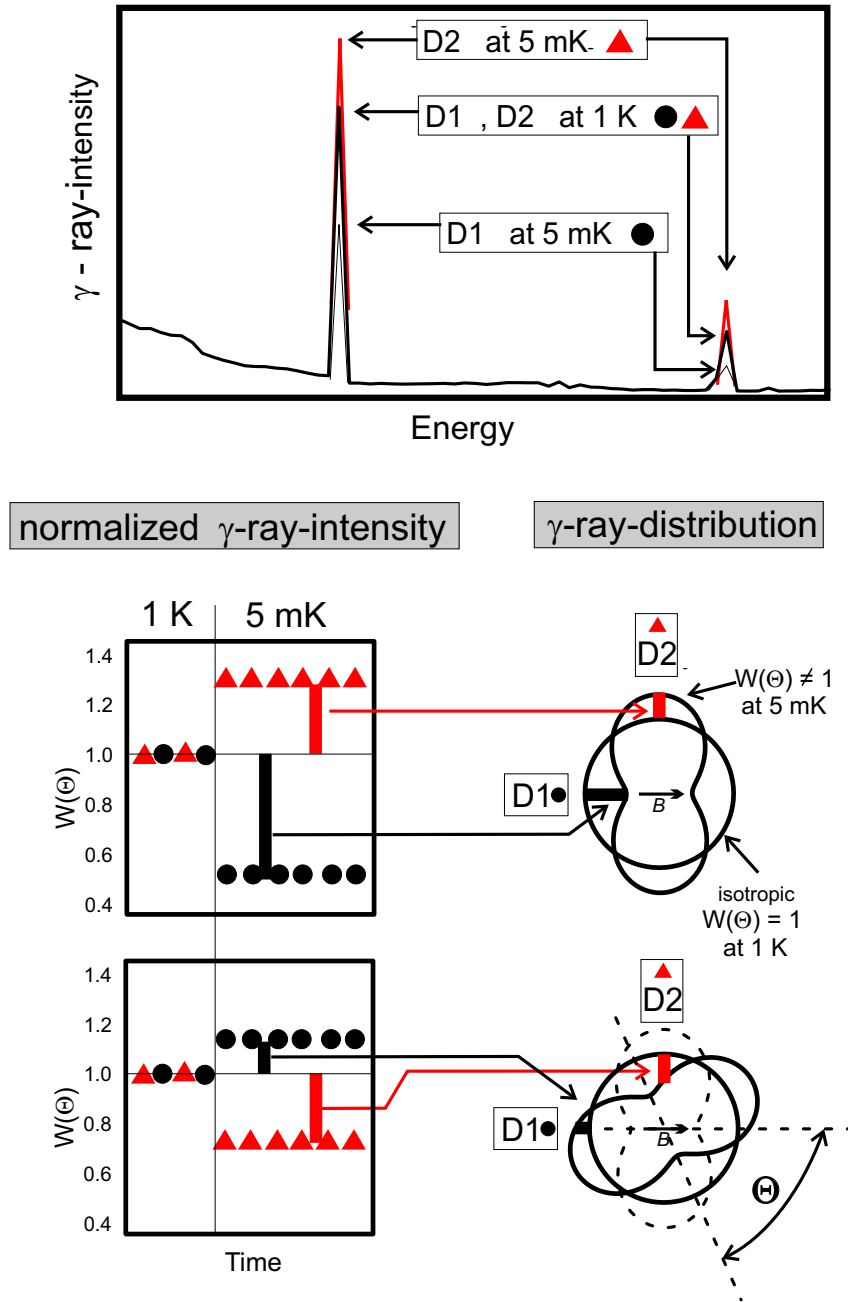
Figure 6.6: Top: Schematic illustrations of γ-ray spectra, which would be measured by the detectors D1 and D2 at 1 K and 5 mK D1(circles). D2(triangle). Center and bottom: normalized γ-ray intensities $W(\Theta)$(left) corresponding to two different γ-ray distributions (right) representing nuclear alignment along two different axes.

6.5   Motivation, results and discussion

6.5.1   Motivation

The original aim of the present LTNO experiments was the investigation of EB trilayers containing a non-magnetic spacer between an FM and an AFM layer. Furthermore, since LTNO is a method which is sensitive to the induced magnetism in the interfacial spacer atoms adjacent to the (anti-)ferromagnetic layers, the spacer can be used as a sensor to study the magnetic coupling at the two interfaces. In order to understand the mechanisms leading to EB, it is crucial to have information about the behavior of the magnetic moments at the AFM interface. This can be achieved by comparing the experimental findings obtained from FM/spacer/AFM EB systems with those obtained from FM/spacer/FM and AFM/spacer/AFM systems.

Therefore, in this chapter LTNO investigations of three different magnetic sample types are presented:

- Co(16.4 nm)/Au(x)/Co(16.4 nm)(FM/spacer/FM) with $x = 0.5$ nm

- CoO(2.0 nm)/Au(x)/CoO(2.0 nm)(AFM/spacer/AFM) with $x = 0.5$, 0.75 nm

- Co(16.4 nm)/Au(x)/CoO(2.0 nm) = (AFM/spacer/FM) = EB system with $x = 0.5$, 0.75 and 1.25 nm

From the γ-ray intensities of ^{60}Co in Co (and CoO) and of ^{198}Au in Au, in an applied magnetic field of 500 mT, i.e. when the ferromagnetic Co is saturated, the magnetic hyperfine fields and the average angle of the nuclear magnetization can be determined. Additionally, hysteresis measurements were performed, detecting the γ-ray intensity as a function of the magnetic field. This is particularly interesting for the case of EB systems, since the ferromagnetic Co layer and the non-magnetic Au interface can be probed at the same time, while the sample is in the EB state. The EB effect has been addressed theoretically by different model calculations. The model proposed by Stiles *et al.* [SM99b] has proved to be well suited to describe the behavior in the present type of granular EB systems. The present results finally will be compared, at least qualitatively, to this model.

6.5.2 Induced nuclear ^{198}Au magnetization in a 0.5 nm thick spacer located in *FM/Au/FM*, *AFM/Au/AFM* and *FM/Au/AFM* trilayers

The normalized γ-ray intensities measured during the cooling of the samples to 5 mK are illustrated in Fig. 6.7 for three different magnetic systems, a) FM/spacer/FM, b) AFM/spacer/AFM and c) FM/spacer/AFM [= EB system], keeping the spacer thickness constant at 0.5 nm. In the present systems FM is: 16.4 nm Co, AFM: 2 nm CoO, spacer: 0.5 nm Au. In Fig. 6.7, the normalized γ-ray intensity at 1 K, $W(\Theta = 1)$, is marked by a flat horizontal line in each plot. Deviations from these lines indicate nuclear alignment.

These measurements were carried out in an applied field of 500 mT, where the FM Co layer is saturated. The γ-ray intensities of ^{60}Co and ^{198}Au were monitored by two fixed detectors D1 ("$0°$ detector", parallel to the applied field axis) and D2 ("$90°$ detector", in-plane perpendicular to the applied field axis) and are plotted in Fig. 6.7 as a function of time (D1: square symbols and D2: cross symbols). A Au thickness of 0.5 nm corresponds to roughly two monolayers of a [111] oriented Au layer, where the monolayer spacing $a_{111} = 0.235\ nm$. On the far right-hand side of this figure, a schematic of the shape of the γ-ray distribution, projected onto the sample plane, is illustrated for both isotopes, ^{60}Co and ^{198}Au. This schematic neglects fourth order contributions and assumes the ensemble of radioactive nuclei to be oriented along an axis at the angle $\pm\Theta$ to the applied field. It is basically given for illustrative purposes. Furthermore, LTNO cannot distinguish $\pm\Theta$. In order not to complicate the schematic diagram of the γ-ray distribution, the shape of the γ-ray distribution $W(-\Theta)$ is not displayed. The black circle represents an isotropic γ-ray distribution, which can be measured at higher temperatures, i.e. at 1 K, where the nuclei are not oriented. The values of the γ-ray intensities at 1 K were used to normalize the values obtained at low temperatures. The solid (dashed) grey "dog-bone" shape outlines the ^{198}Au (^{60}Co) γ-ray distribution at low temperatures. The orientation of the "dog-bone" shape indicates the in-plane direction of the nuclear alignment with respect to the applied field. The γ-ray distribution of ^{60}Co in the Co/Au/Co trilayer and in the Co/Au/CoO EB-system was observed to be anisotropic, indicating nuclear alignment. In contrast, for the case of ^{60}Co in CoO in the (CoO/Au/CoO), system no γ-ray anisotropy was observed during the cool-down (see Fig. 6.7b). Thus the γ-ray intensity is isotropically distributed and remains unchanged from the high-temperature γ-ray distribution.

In comparison to ^{60}Co, the ^{198}Au γ-ray distribution shows a different behavior. For the Co/Au/Co trilayer and the EB system, the γ-ray intensity
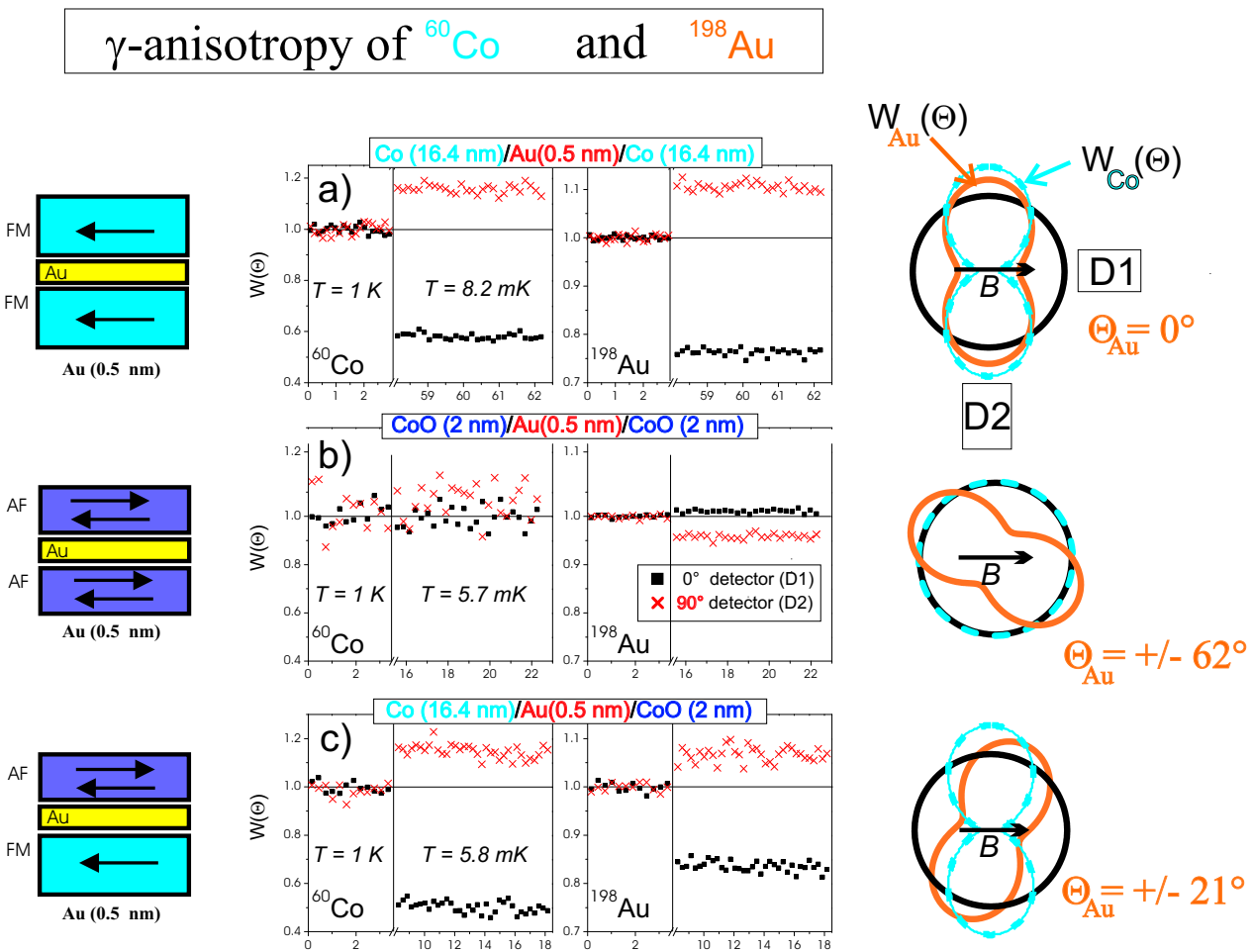
Figure 6.7: Normalized γ-ray intensity for three different magnetic systems: Co/Au/Co (a); CoO/Au/CoO (b); Co/Au/CoO (EB) (c), each with a 0.5 nm Au spacer. Right: schemes of the γ-ray distribution, projected onto the sample plane, for the case of (i) an isotropic distribution (black solid line) and (ii) for nuclear alignment ("dog-bone" shape) parallel to the field (grey dashed lines) and at an angle with respect to the field (grey solid lines).

Au(0.5 nm) in	$\pm\Theta_{Au}$	Average hyperfine field B_{HF} [T]
Co/Au/Co	0	78(3)
CoO/Au/CoO	62(3)	23(2)
Co/Au/CoO	21(4)	48(4)

Table 6.2: *Average angle Θ_{Au} of the nuclear alignment of the Au moments with respect to the applied field axis in a 0.5 nm thick Au spacer, sandwiched between two magnetic layers, and the average Au hyperfine field ("one site model") for three different magnetic sample types: FM/Au/FM, FM/Au/AFM (EB system), and AFM/Au/AFM, with FM = Co and AFM = CoO.*

detected by D1 (D2) decreased (increased) during the cool-down. A drastic reorientation of the Au moments was observed for the Au moments in CoO/Au/CoO, where the γ-ray intensity was found to increase (decrease), as measured by D1 (D2). That is, in comparison to the two other systems, the intensity deviations with respect to the warm-countrate intensity are rotated, indicating a significant canting angle Θ of the nuclear alignment. This situation is schematically illustrated in Fig. 6.6. From the γ-ray anisotropy $W(\Theta)$, the average hyperfine fields were determined. From the ratio of the intensity deviations from $W(\Theta)=1$, as measured by two fixed detectors, the average angle $\pm\Theta$ could be determined (see table 6.2).

The average nuclear alignment of the Au in the Co/Au/Co trilayer was found to be parallel to the applied field, while an average angle of $\Theta = 62°$ was observed for the Au moments in the CoO/Au/CoO systems. For the EB system, a small canting of $\Theta = 21°$ was extracted from the ratio of the two measured γ-ray intensities.

Although a nuclear thermometer ([54]Mn in Ag) was used to control the temperature during the experiment, the temperature of the layer systems investigated, containing a FM Co-layer, can also be determined directly from the [60]Co γ-ray intensity emitted from the sample. Since the hyperfine field of ^{60}Co in Co is well known ($B_{HF} = -21.63$ T [ZHEE78]), the [60]Co γ-ray anisotropy, as well as the nuclear thermometer, gives the correct sample temperature. As plotted in Fig. 6.7, the sample temperature of the Co/Au/Co sample (a) was 8.2 mK, while it was 5.8 mK during the experiment with the Co/Au/CoO EB-trilayer (c). Using this temperature, an average hyperfine field for the Au was determined and is given in table 6.2.

In summary, two basic trends have been observed, shown in table 6.2: the average angle Θ between the hyperfine field and the applied saturated field is canted further away from 0° by replacing the Co interfaces with CoO interfaces,

while the average hyperfine field on the Au nuclei decreases.

In the following sections, the different magnetic sample types will be treated separately in order to further explore the nature of the Au nuclear magnetization at different magnetic interfaces. For the cases of the CoO/Au/CoO and the Co/Au/CoO systems, samples with thicker Au spacers have been investigated. In addition, hysteresis measurements have been performed, detecting the ^{60}Co and ^{198}Au γ-ray anisotropies as a function of the external field.

6.5.3 *FM/spacer/FM*: γ-ray anisotropies of ^{60}Co and ^{198}Au in Co(16.4 nm)/Au(x)/Co(16.4 nm) with $x = 0.5$ nm

The results obtained from the AFM/Au/AFM and the FM/Au/AFM EB trilayers (see next paragraphs) should be compared to the behavior of a simple FM/spacer/FM system prepared under similar experimental conditions. In order to get information on the Au/Co interface, Co/Au/Co trilayers were investigated. The normalized γ-ray intensities for a simple Co/Au/Co trilayer, prepared in a similar manner as described in chapter 3, are plotted in Fig. 6.7a. As discussed in the first paragraph of this section, the hyperfine fields of the Au and Co were aligned along the applied field in saturation (see Fig. 6.7a). The average Au hyperfine field amounts to 78(3) T (see also table 6.2). This magnitude is surprisingly close to the hyperfine field of 87.02(11) T known for ^{198}Au as an impurity in fcc Co ([EEH$^+$86] and [SP86]). Since the technique of LTNO is sensitive only to the alignment of the interfacial Au, this result suggests that there is a large number of Au atoms in the [Au(0.5 nm)] layer with more than one Co neighbor.

In summary, the interfacial Au in Co/Au/Co was found to be aligned with the magnetically saturated FM Co. Furthermore, the hyperfine field at the Au near Co/Au interfaces was found to approach a value close to that obtained for Au as an impurity in Co, indicating that for this Au spacer, pinholes are predominant.

6.5.4 *AFM/spacer/AFM*: γ-ray anisotropies of ^{60}Co and ^{198}Au in CoO(2 nm)/Au(x)/CoO(2 nm) with $x = 0.5, 0.75$ nm

In order to investigate the CoO/Au interface, similar experiments on two CoO/Au(x)/CoO trilayers with varying Au-layer thicknesses $x = 0.5$, 0.75 nm were performed. Both samples were prepared at the same time and under

exactly the same conditions, to ensure that all preparation parameters were the same, except the Au spacer thickness. Before top-loading the sample into the cryostat, a field of about 600 mT was externally applied to the sample to simulate the procedure applied to the EB systems. During the cool-down from 4 K to mK temperatures, a constant field of 500 mT was applied.

The cool-down curves of the ^{198}Au γ-ray intensities are plotted in Fig. 6.8 as a function of time for the two samples, down to a base temperature of 5.7 mK. The normalized γ-ray intensity at 1 K, $W(\Theta = 1)$, is marked by a flat horizontal line in each plot. Deviations from this lines indicate nuclear alignment. A schematic of the in-plane projections of the γ-ray distributions is given on the right-hand side of the figure for both isotopes. In this figure, the cool-down curve for the trilayer containing 0.5 nm Au is repeated (see Fig. 6.7b) for clarity.

An observable γ-ray anisotropy (= deviation from $W(\Theta) = 1$) of the ^{198}Au was detected for both samples (see Fig. 6.8), while no γ-ray anisotropy from the ^{60}Co (in CoO) was observed at low temperatures ($W(\Theta) \sim 1$). The normalized ^{60}Co (in CoO) γ-ray intensity is shown in Fig. 6.7b for the sample containing 0.5 nm Au, while the result for the ^{60}Co γ-radiation (from Co in CoO) for the sample with the 0.75 nm thick Au layer is not displayed. A schematic of the in-plane projection of the γ-ray distribution of ^{198}Au is given on the right-hand side of Fig. 6.8. The nuclear spin-lattice relaxation (NSLR) time for ^{198}Au can be estimated from the cool-down curve to be less than 15 minutes, while for ^{60}Co (in CoO) it is either very long, or else the ^{60}Co is not oriented in CoO (to be discussed later).

γ-ray anisotropy of ^{198}Au in $CoO/Au(x)/CoO$

From Fig. 6.8, the cooling curves of the ^{198}Au γ-ray intensities for both samples will be compared in the following, using the data from the two in-plane detectors D1 (="0°detector" parallel to the external field) and D2 (="90°detector" in-plane, perpendicular to the external field). A drastic change in the nuclear Au spin polarization was observed as the Au spacer thickness was varied. In Fig. 6.8, the γ-ray anisotropy measured by D2 (crosses) for both samples is $W(\Theta) < 1$, while the γ-ray anisotropy measured by D1 (squares) is $W(\Theta) > 1$ for the sample with Au(0.5 nm) and $W(\Theta) < 1$ for the sample with Au(0.75 nm), indicating a significant reorientation of the nuclear spin polarization induced in the Au layer. Taking the ratio of the γ-ray anisotropies measured by the two detectors (D1, D2), the in-plane angles between the axis of the average alignment of the nuclear Au moments and the axis of the applied field were determined; see table 6.3. In the case of Au, this angle is approxi-
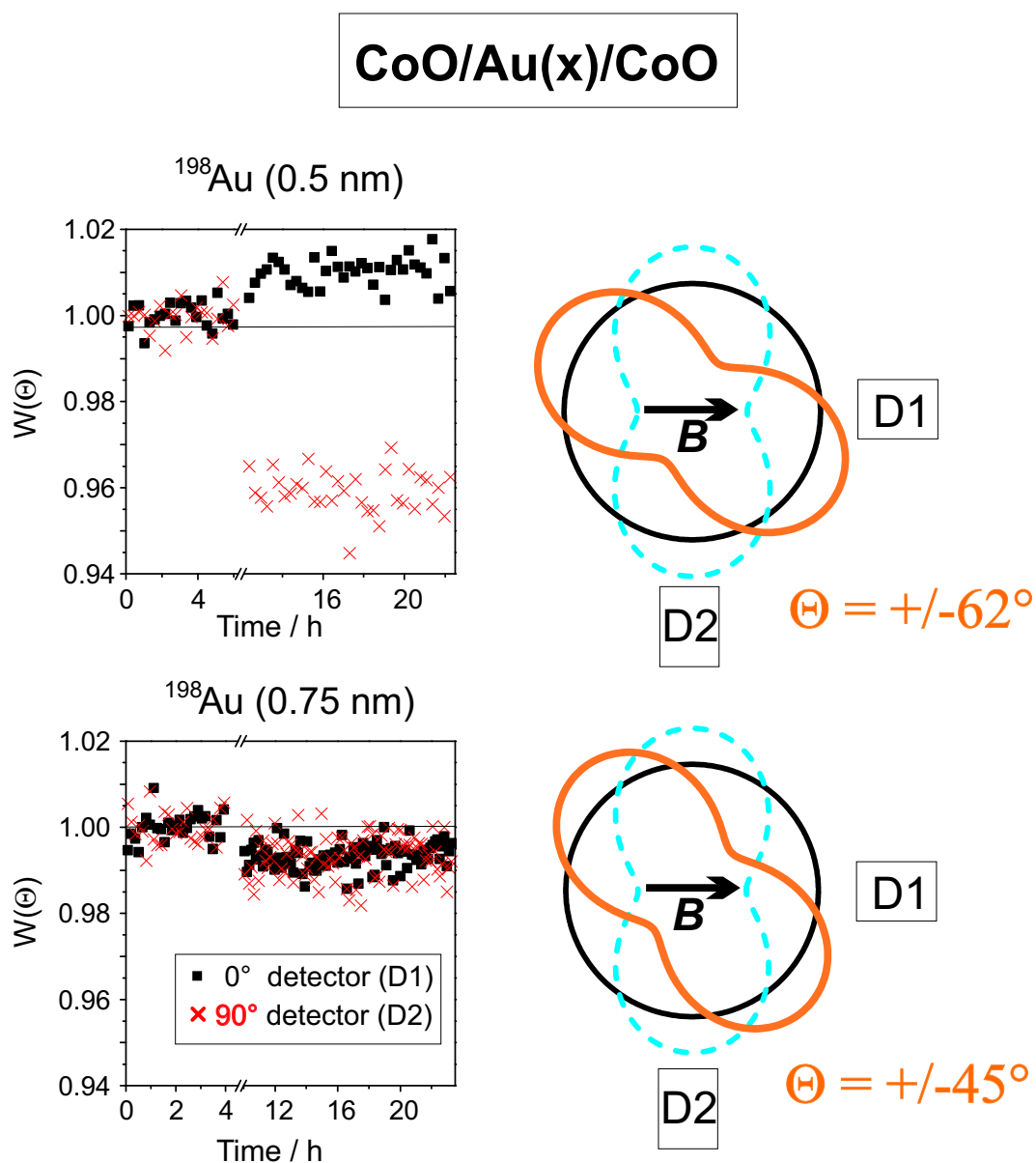
CoO/Au(x)/CoO

^{198}Au (0.5 nm)

^{198}Au (0.75 nm)

■ 0° detector (D1)
✕ 90° detector (D2)

Figure 6.8: Left: normalized γ-ray intensity for CoO(2 nm)/Au(x)/CoO(2 nm), with $x = 0.5, 0.75$ nm, measured by the detectors D1 (squares) and D2 (crosses); Right: scheme of the γ-ray distribution, projected onto the sample plane, for the case of (i) an isotropic distribution (black solid line) and (ii) for nuclear alignment ("dog-bone" shape) parallel to the field (grey dashed line) and at an angle with respect to the field (grey solid line).

Au-thickness x in nm for CoO/Au(x)/CoO	$\pm\Theta_{Au}$	average hyperfine field B_{HF} [T] ("one site model")	"interfacial" hyperfine field B_{HF} [T] ("two site model")
0.5	62(3)	23(2)	24(2)
0.75	45(2)	16(2)	21(2)

Table 6.3: *Average angle Θ_{Au} of the nuclear alignment of the ^{198}Au moments in an Au spacer sandwiched between two AFM CoO layers with respect to the applied field axis. The average hyperfine field ("one site model") and the hyperfine field calculated with the assumption that strong Au polarizations are restricted to the CoO/Au interface ("two site model"), are given for two different Au spacer thicknesses, $x = 0.5$ nm and 0.75 nm*

mately temperature independent (4th order contribution to $W(\Theta)$ is negligible) in the temperature range considered. Using the data from the two detectors (D1, D2), the nuclear spin orientation for the sample with [Au(0.5 nm)] was determined to be largely in-plane. As given in the table, the average in-plane angle, relative to the applied field axis, was found to be $\pm62(3)°$ at 500 mT. The sign of the angle is unknown since γ-decay conserves parity and cannot be used to determine the sense in which the spins are directed along a particular axis. In contrast, for the sample with [Au(0.75 nm)], the nuclear spin orientation of the Au moments was observed to rotate to an in-plane angle of $\pm45(2)°$, by using three detectors (data from the third detector, which was positioned perpendicular to the sample plane, are not shown in the figure).

The average Au hyperfine field ("one site model"), as given in table 6.3, was calculated assuming that both samples were near the base temperature of the cryostat. For the CoO/Au/CoO trilayers, the sample temperature was taken from the ^{54}Mn in Ag thermometer.

A drastic reduction of the average hyperfine field B_{hf} from 23(2) T to 16(2) T was observed as the Au-spacer thickness increased from 0.5 nm to 0.75 nm. This can also be expressed as a reduction in the degree of nuclear spin alignment by a factor of $\frac{B_2[Au(0.75\ nm)]}{B_2[Au(0.5\ nm)]} = 0.54$.

As opposed to the "one site model", assuming instead that only Au sites directly adjacent to the CoO interface experience a nonzero hyperfine field, i.e. applying a "two site model", the average Au hyperfine fields for these sites were recalculated for both samples. The values (24(2) T [Au(0.5 nm)] and 21(2) T [Au(0.75 nm)]) are given in the right column of table 6.3. A comparison of the results for the hyperfine fields B_{hf} indicates that the "two site model" is

confirmed, since the hyperfine field values at the CoO/Au interfaces are within the error bars equal for the two samples, while the average hyperfine field (i.e. "one site model") decreases with increasing Au spacer thickness. Thus, it can be concluded that strong polarizations of the nuclear Au moments are largely restricted to the interface atomic layers.

γ-ray anisotropy of ^{60}Co in $CoO/Au(x)/CoO$

As already mentioned, in the case of ^{60}Co (in CoO), no detectable γ-ray anisotropy was observed for both samples and by both detectors (D1, D2) ($W(\Theta) \approx 1$), as plotted for the sample with [Au(0.5 nm)] in Fig. 6.7b as a function of time. In contrast to the present result, the hyperfine field at Co in bulk CoO was determined to be +49.5 T by Okada and Yasuoka using NMR [OY77] (for calculations of B_{HF} see also [Mot60]); thus the γ-ray anisotropy for a CoO sample, fully aligned along the applied field at 5.7 mK in thermal equilibrium, would be expected to amount to $W(0°) = 0.09$. However, if the NSLR time for ^{60}Co (in CoO) is very long at these temperatures, then, over a measurement period of about one week, little or no ^{60}Co γ-ray anisotropy is expected to be observed. Estimates for the nuclear spin relaxation time of ^{60}Co in these CoO films are difficult to obtain. The NSLR times of ^{60}Co in bulk CoO should be of the order of weeks for the following reasons: phonons cannot make a significant contribution to the relaxation, since they are hardly excited at these temperatures and only weakly coupled to the nuclear moments. For non S-state ions, the magnon energy gap E_g is comparable to kT_N [Jac], in this case $T_N = 300$ K for CoO. Considering that nuclear spin relaxation times of 38 days have been reported for MnCl$_2$.4H$_2$O below 60 mK [GKT93], which has an energy gap of $E_g/k \sim 1$ K, then for the nuclear spin relaxation of ^{60}Co in bulk CoO similar, if not greater, relaxation times could be expected. Another possible reason for observing zero ^{60}Co γ-ray anisotropy is that on average the CoO grains are not magnetically aligned. It should be noted that the ^{60}Co (in CoO) signal is not exclusively emitted only from the CoO/Au interface, but is averaged over the whole CoO layer. In contrast to this, the anisotropic γ-radiation from the Au is emitted mainly from the interface, where significantly large hyperfine fields are present. The fact that the Au has achieved some alignment at the interface implies that the Co ions in CoO at the same interface are at least partially aligned.
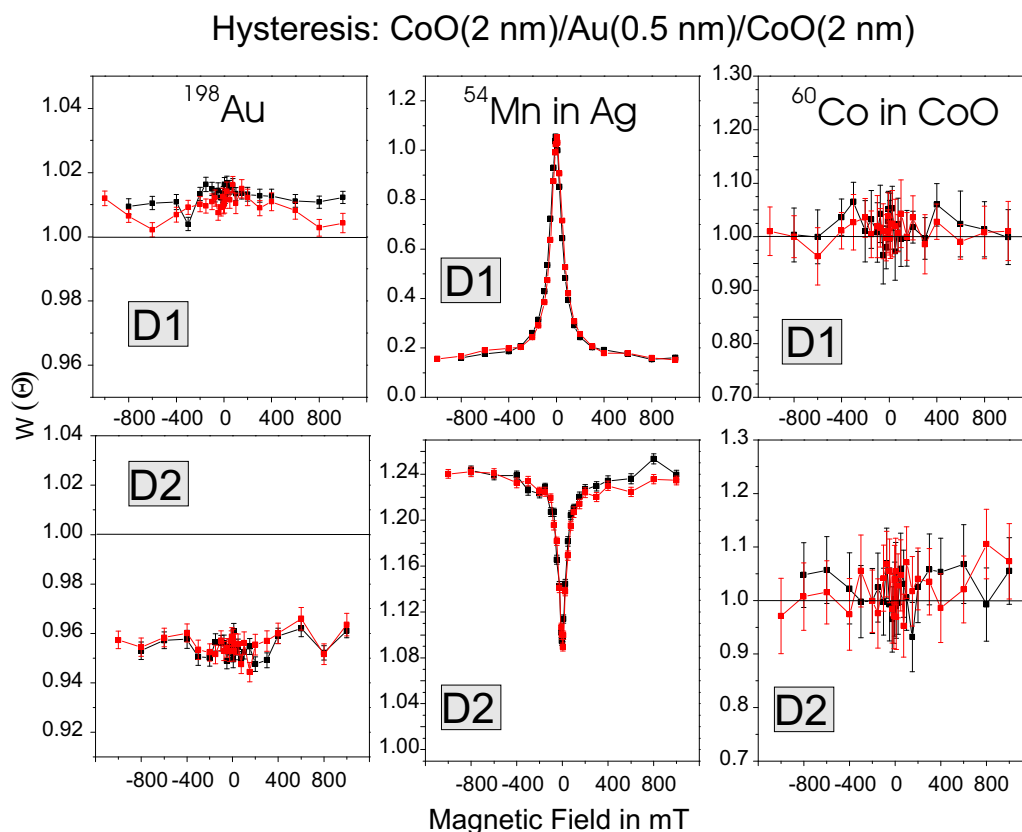
Figure 6.9: γ ray-anisotropy $W(\Theta)$ for ^{198}Au and ^{60}Co in CoO/Au/CoO and of the ^{54}Mn in Ag thermometer (middle); 0°(top) and 90° (bottom) detectors.

Hysteresis measurements of ^{198}Au and ^{60}Co γ-ray anisotropies in a $CoO/Au/CoO$ trilayer

In addition, hysteresis measurements were performed by measuring the γ-ray intensity from ^{60}Co in CoO and ^{198}Au in Au as a function of the applied field (see Fig. 6.9). Within error bars the detected intensities for both isotopes do not change significantly as a function of the applied field.

This result indicates, within the experimental accuracy, that the Co nuclear moments in AFM CoO and the Au nuclear moments at the CoO/Au interface appear not to reorient within an external field range between $\pm$ 1 T. The data from the nuclear thermometer ^{54}Mn in Ag, also plotted, demonstrate that there were no major temperature fluctuations in the cryostat during the experiment.

In summary, a drastic change in the polarization of the Au nuclear moments in CoO/Au(x)/CoO has been observed as the Au spacer thickness is increased. Furthermore, it could be confirmed that large polarizations of the Au nuclear moments are restricted to the interface atomic layers. The results for Au indicate that the Co ions in interfacial CoO have to be at least partially aligned, although the γ-ray distribution from Co in CoO is isotropic within experimental sensitivity. This can be attributed either to magnetically non-aligned CoO grains and/or to very long NSLR times for Co in CoO at low temperatures. Additionally, the interfacial Au and Co nuclear moments appear not to reorient significantly up to applied fields of ± 1 T.

6.5.5 *FM/spacer/AFM*: γ-ray anisotropies of ^{60}Co and ^{198}Au in Co(16.4 nm)/Au(x)/CoO(2 nm) with $x = 0.5, 0.75, 1.25$ nm

In this section, the investigation of three different Co/Au(x)/CoO EB-trilayers with increasing Au-spacer thicknesses, $x = 0.5, 0.75$, and 1.25 nm will be presented. The samples where again prepared at the same time, under the same conditions and varying only the Au layer thickness. Before the samples where introduced into the cryostat, they were subjected to an external field of 600 mT to induce EB. During the cooling from approximately 4 K to base temperature in the samples' remanent state, an external field of 500 mT was applied.

The cool-down curves of both the ^{198}Au (right-hand side) and ^{60}Co (left-hand side) γ-ray intensities are plotted in Fig. 6.10 as a function of time for the three samples.

The normalized γ-ray anisotropy at 1 K, $W(\Theta) = 1$, is marked by a flat horizontal line in each plot. Deviations from these lines indicate nuclear alignment. A schematic of the in-plane projections of the γ-ray distributions is given on the far right-hand side of the figure for both isotopes.

For these measurements, the sample temperature could be determined directly from the ^{60}Co in Co γ-ray anisotropy, since the hyperfine field of ^{60}Co in fcc Co is well known (see also 1st paragraph of this section).

The temperatures measured from the "internal" ^{60}Co thermometer for each sample were 5.8, 6.6, and 14.25 mK for samples with Au thickness of 0.5 nm, 0.75 nm, and 1.25 nm, respectively. Since the thermal contact between the cryostat cold finger and the sample was not equally good in each experiment, differences in the base temperature are to be expected.
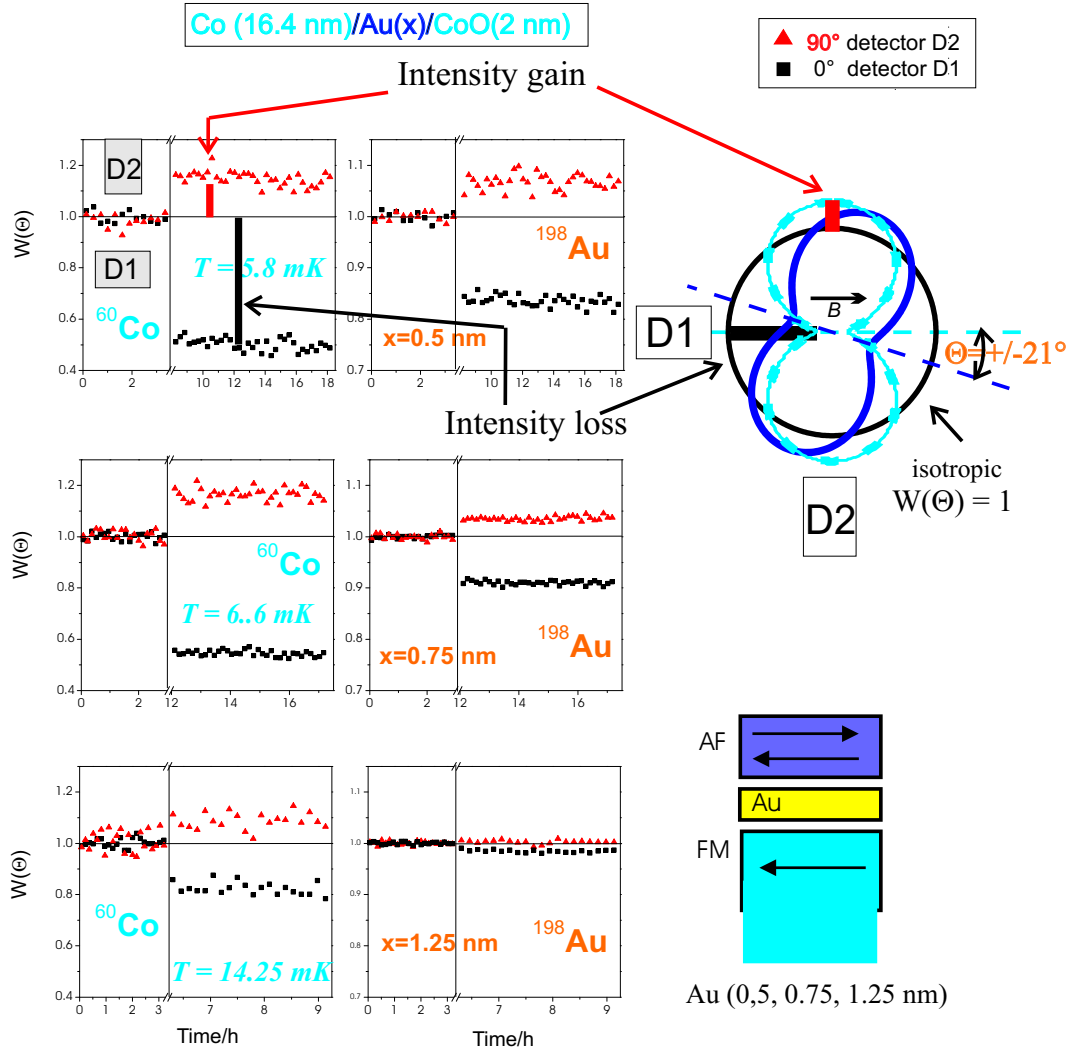
Figure 6.10: γ-ray anisotropy $W(\Theta)$ for three different EB systems, Co(16.4 nm)/Au(x)/CoO(2.0 nm) with $x = 0.5, 0.75$, and 1.25 nm in a field of 500 mT, where the ferromagnetic Co is magnetically saturated. On the far right-hand side a schematic is given showing possible γ-ray distributions: isotropic distribution at 1 K (black circle); anisotropic distributions at mK temperatures for the case of nuclear alignment along the applied field axis ("dog bone" shape; grey dashed line) and for the case of nuclear alignment along an axis which is canted with respect to the applied field ("dog bone" shape; solid line).

γ-ray anisotropy of ^{198}Au in $Co/Au(x)/CoO$

The cooling curves, plotted in Fig. 6.10, of the ^{198}Au γ-ray anisotropies for the three EB samples with increasing Au layer thickness will be compared in the following paragraph, using the data from the two in-plane detectors D1 (="0°detector" parallel to the external field) and D2 (="90°detector" in-plane, perpendicular to the external field).

From Fig. 6.10, the maximum γ-ray anisotropy from the Au layer at saturation was found to decrease with increasing Au thickness. That means that the ^{198}Au γ-ray intensities, measured by both detectors (D1, D2), approach the value $W(\Theta) = 1$, as the spacer thickness is increased.

The in-plane angles Θ_{Au} for the nuclear alignment of the Au moments with respect to the external field axis were determined and are given in table 6.4. From the data, an in-plane angle Θ_{Au} of about 21° for the nuclear alignment of the Au moments was found for the two samples having good thermal contact. The in-plane angle for the Au nuclear moments in the sample with [Au(1.25 nm)] was found to be larger; however, because of the poor signal-to-noise ratio during this experiment, the error bars were significantly larger. Nevertheless, it should be stressed that for all three EB systems the nuclear magnetization was found to be canted with respect to the applied field (500 mT). Comparing this result to that obtained for AFM CoO/Au/CoO trilayers, where significant canting angles for the interfacial Au have been found, the present results can only be attributed to the influence of the CoO upon the interfacial nuclear Au moments. The observed canting of the nuclear Au alignment is much smaller for the EB systems than for the CoO/Au/CoO trilayers (for comparison see tables 6.3 and 6.4). The degree of canting appears to increase with the number of CoO/Au interfaces. The CoO/Au/CoO samples both have a larger degree of canting than the EB systems. As has been described, the Au nuclear moments at an FM-Co/Au interface are aligned with the FM Co, see Fig. 6.7 and table 6.2. Thus, averaging the contributions arising from the two different interfaces in an EB system, the canting angle is expected to be reduced in comparison to the angle found for the system with two CoO/Au interfaces.

Determining the sample temperatures from the ^{60}Co γ-ray anisotropy, the average hyperfine fields for all three samples have been calculated (i.e. applying the "one site model"). The results are given in table 6.4. The hyperfine fields are assumed to be distributed uniformly across the Au layers and were found to be 48(4), 37(1) and 37(13) T for the samples with (0.5 nm), (0.75 nm) and (1.25 nm) Au layers, respectively. The average Au hyperfine field ("one site model") is reduced as the Au spacer thickness is increased. From these results on the first two samples, it can be concluded that the hyperfine fields of the Au

Au-thickness x in nm for Co/Au(x)/CoO	$\pm\Theta_{Au}$	average hyperfine field B_{HF} [T] ("one site model")
0.5	21(4)	48(4)
0.75	21(2)	37(1)
1.25	32(5)	37(13)

Table 6.4: *Average angle Θ_{Au} of the nuclear alignment of the ^{198}Au moments in a Au spacer sandwiched between the FM Co layer and the AFM CoO layer, with respect to the applied field axis, and the average hyperfine field ("one site model") are given for three different Au spacer thicknesses $x = 0.5, 0.75$, and 1.25 nm.*

layers are restricted to the interface layers adjacent to the magnetic material. Unfortunately, the sample with the (1.25 nm) Au layer had poorer thermal contact and a thicker Au layer –both leading to a reduced signal to noise ratio. In a thicker Au layer, the contribution of the "inner" layers (i.e. 62% of the whole layer for the sample with (1.25 nm) Au) are expected to further reduce the average γ-ray anisotropy observed. From these data it can be established that large polarizations of the Au nuclear moments are limited only to the Au interfaces, as has also been found by [RDF+97] and [KNES94].

γ-ray anisotropy of ^{60}Co in *Co/Au(x)/CoO*

As stated in the first paragraph of this section, the hyperfine field of ^{60}Co in FM fcc Co is well known and amounts to 21.63 T. Thus, in the case of the EB systems, the ^{60}Co (in FM Co) γ-ray anisotropy is used to determine the temperature directly from the sample. Here, the $\sim 10\%$ of the total γ-ray radiation resulting from ^{60}Co within the CoO layer is assumed to be isotropic, as was measured in thin CoO/Au/CoO trilayers (see previous paragraph). The in-plane angle of the ^{60}Co nuclear magnetization was determined with respect to the applied field (500 mT). As was to be expected for FM Co, it was found to be aligned along the external field.

Hysteresis measurements of ^{198}Au and ^{60}Co γ-ray anisotropies in *Co/Au(x)/CoO* EB trilayers

In order to observe the induced EB effect with LTNO, hysteresis measurements were performed, detecting the γ-radiation emitted by the radioactive probes ^{60}Co and ^{198}Au in the three EB systems as a function of the applied field.
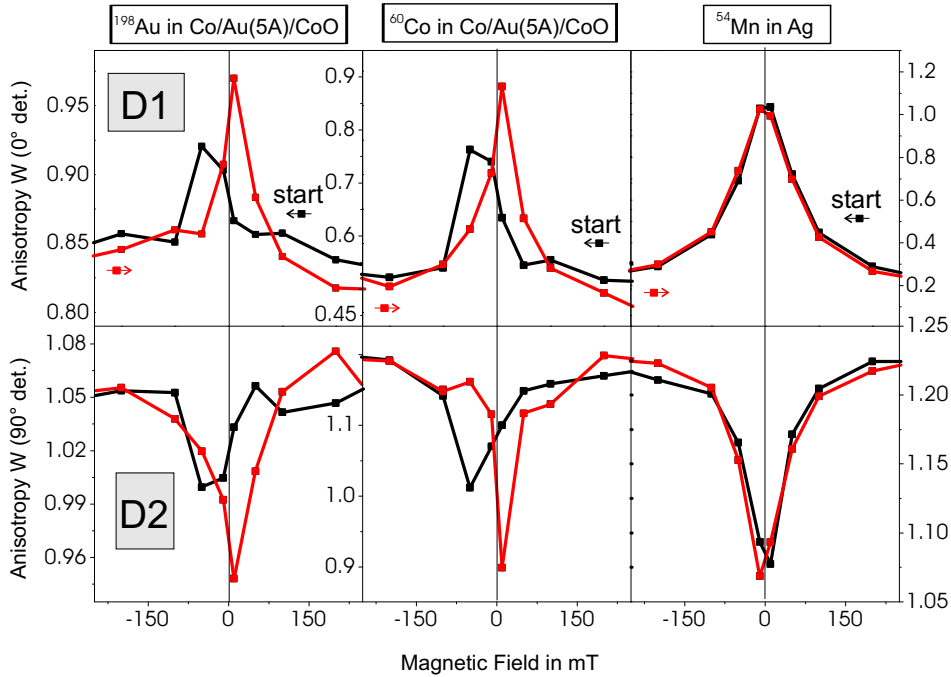
Figure 6.11: Hysteresis measurement: normalized γ-ray intensity of ^{60}Co and ^{198}Au in the EB state, and the ^{54}Mn in Ag thermometer, as a function of the applied field.

Since all samples where previously cooled from the remanent magnetization state, they are in the EB state when the cryostat is at its base temperature of 5 mK. The hysteresis was usually started at +500 mT, i.e. with the applied field parallel to the initial magnetization field, except for the sample with [Au(0.75)nm], which was started at -500 mT. The aim was to observe the EB effect through the polarization of the nuclear magnetization of ^{60}Co, and particularly that of the interfacial ^{198}Au, since many other common techniques are not sensitive to the induced magnetism in noble metal spacers. Fig. 6.11 shows the normalized γ-ray intensities monitored by both detectors (D1, D2) for ^{198}Au (left) and ^{60}Co (middle), emitted from the Co/Au(0.5 nm)/CoO tri-layer as a function of the applied field (hysteresis). Additionally, the ^{54}Mn in Ag (right) γ-ray intensities are plotted for comparison. The γ-ray intensity of the ^{54}Mn in Ag thermometer shows a completely symmetric curve for positive and negative applied fields (Fig. 6.11 right). Furthermore, there was no difference between the γ-ray intensities measured at increasing and decreasing applied magnetic fields for the ^{54}Mn in Ag nuclear thermometer. On the other hand, the ^{60}Co and ^{198}Au radiations show a striking asymmetry in the size of

the observed maxima and minima. This asymmetry can thus not be due to temperature effects, and must instead be attributed to the EB effect.

In Fig. 6.12, the γ-ray intensities, measured by D1, of ^{198}Au (left) and ^{60}Co (in Co) (right), are summarized for the three EB systems with increasing Au spacer thicknesses (0.5, 0.75, 1.25 nm). The result for the sample with [Au(0.5 nm)] is repeated for clarity (see 6.11).

For both the ^{60}Co **and** the ^{198}Au γ-ray anisotropies, two maxima are observed at smaller magnetic fields, –i.e. when the sample is not saturated and when the magnetization reversal takes place–, one on each side of the zero field axis but not symmetrical with respect to $B = 0$. Comparing the curves obtained for ^{60}Co and ^{198}Au γ-ray intensities, it is obvious that the interfacial Au nuclear moments are strongly polarized by the neighboring Co atoms. The Au nuclear magnetization follows the FM Co magnetization during the magnetization reversal process, leading qualitatively to the same dependence of the γ-ray intensity on the external field. The only differences are the absolute values of the normalized γ-ray intensities, which have been discussed in the previous paragraph for the case of magnetic saturation.

The average of the two maxima is shifted towards negative fields, as expected for an exchange bias system previously cooled in a positive cooling field. Taking the strength of the exchange bias to be the average of the two maxima, the measured exchange bias fields are found to be 20, 12 and 8 mT for Au thicknesses of 0.5, 0.75, and 1.25 nm, respectively (Fig. 6.12). Considering the fact that the samples were cooled from their remanent state, these exchange bias fields agree within experimental accuracy with those previously measured by SQUID magnetometry at 10 K [GGR01] on the same samples. Furthermore, they decrease in strength as expected for increasing Au thickness (for further details see chapter 4). From the results in chapter 4, obtained by SQUID magnetometry, it was found that the strength of the EB field decreases nearly linearly as the spacer thickness is increased. For the present experiments this could not be expected, because the hysteresis curve of the sample with [Au(0.75 nm)] was started from a negative field, i.e. antiparallel to the remanent magnetization and to the direction of the induced exchange bias.

The effect of this procedure, as well as the effect of zero-field cooling from the remanent state, on the hysteresis of an EB sample, has been measured by SQUID magnetometry for a simple Co/CoO system at 10 K. The results are shown in Fig. 6.13. The hysteresis was usually started at a saturation field pointing in the direction of the remanent magnetization (i.e. the direction of the induced EB). Except for the reduction of the EB, the hysteresis loop of the zero-field-cooled sample is more strongly curved in contrast to the sample which was field cooled in a field of 400 mT. In a second measurement, an EB
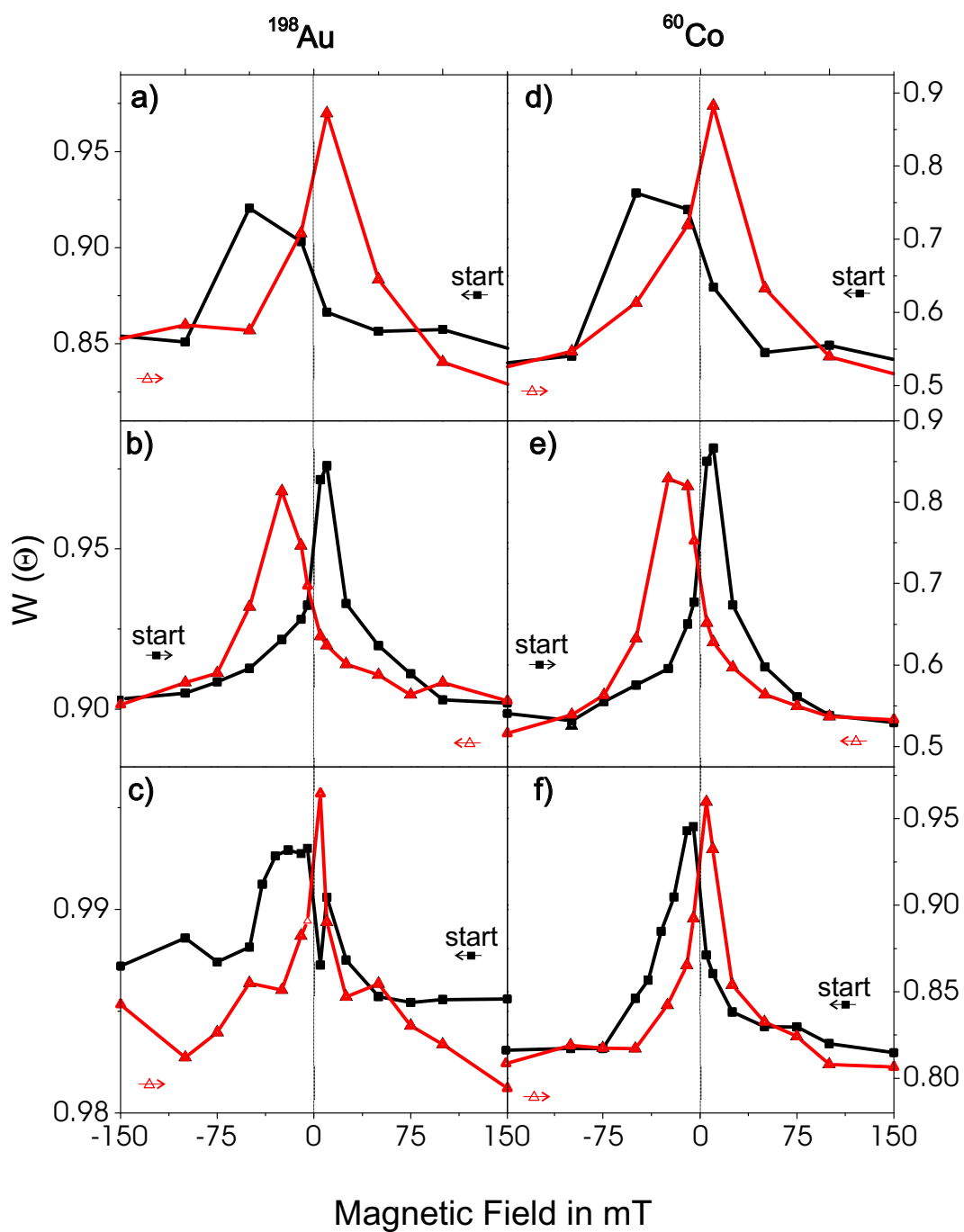
Figure 6.12: Hysteresis of the Co(16.4 nm)/Au(x nm),/ CoO(2.0 nm) from both the ^{60}Co and ^{198}Au radioactive probe nuclei with (a) and (d): 0.5 nm Au, (b) and (e): 0.75 nm Au, (c) and (f): 1.25 nm Au spacer layers.
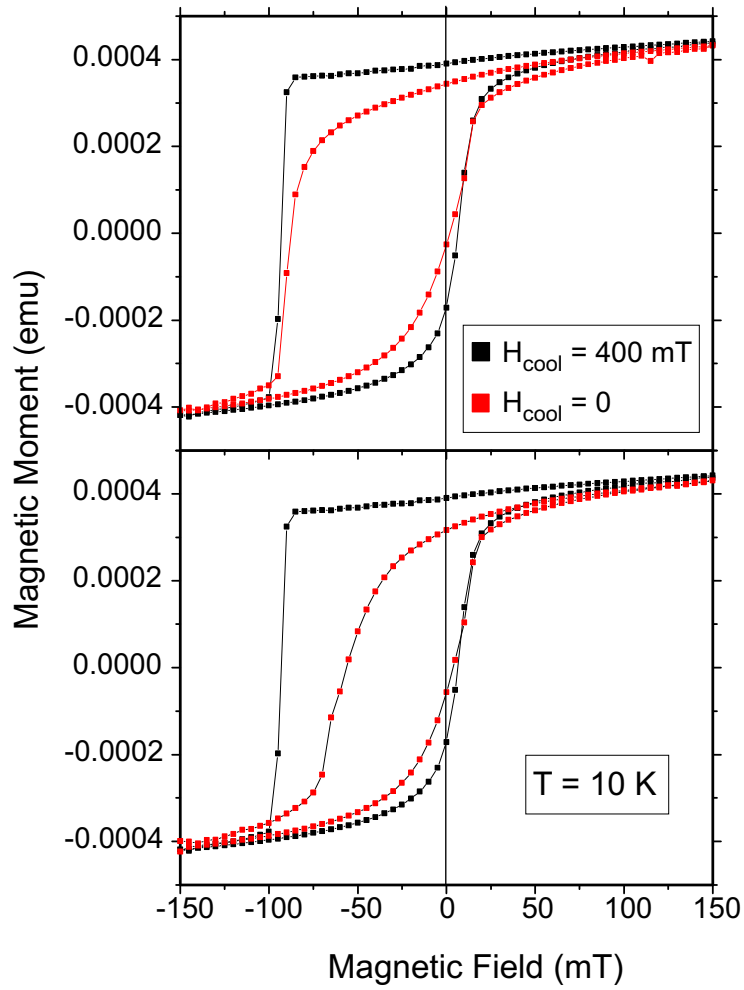
Figure 6.13: SQUID measurements of a Co/CoO bilayer field-cooled in $H_{cool} =$ 400 mT (black squares) and (i) zero-field cooled from the remanent state (top, grey squares) and (ii) zero-field cooled from the remanent state starting the hysteresis from a field opposite to the remanent field direction (bottom, grey squares).

sample was again cooled in zero-field from the remanent state. The hysteresis curve was then started from the saturated state opposite to the direction of the remanent magnetization (plotted in the bottom part of Fig. 6.13). This procedure is equivalent to a training process. In addition to the rounding on both sides of the hysteresis loop, which was also observed in zero-field cooling, a drastic reduction of the EB effect was observed. This is similar to the training effects which can be observed in many EB systems.

Thus, a training procedure seems to be responsible for the reduced EB field which was obtained for the [Au(0.75 nm)] sample using LTNO.

As described above, the signal-to-noise ratio is poor for the ^{198}Au γ-ray anisotropy measured for the sample with the thickest Au spacer [Au(1.25 nm)], and thus the shape of the curve plotted in Fig. 6.12 is somewhat erratic compared to the other two samples. Nevertheless, even for this sample the asymmetric shift of the center between the two γ-ray intensity maxima with respect to the zero field axis can be observed.

In summary, it has been established that the Au nuclear magnetization in Co/Au/CoO EB systems is canted with respect to the applied field in saturation. In comparison with the results obtained for CoO/Au/CoO trilayers, this canting is induced at the CoO/Au interface, while the interfacial Au at the Co/Au interface is expected to be aligned along the applied field at saturation. Furthermore, it was confirmed that large polarizations of the Au nuclear moments in the EB systems are restricted to the interfaces with magnetic layers . Performing hysteresis measurements on three EB samples in the EB states demonstrates that the EB effect can be observed in the Co nuclear magnetization **and** in the induced magnetism of the interfacial Au atoms. The induced nuclear alignment of the Au moments appears to simply follow the magnetization reversal of the Co moments in hysteresis curves.

6.5.6 Magnetization reversal in a *Co/Au/CoO* EB trilayer measured by the nuclear probe isotopes ^{60}Co and ^{198}Au

Apart from the fact that EB can be observed via LTNO in an FM Co layer and in the adjacent interfacial non-magnetic Au, the method can potentially also be used to study the magnetization reversal processes occurring in the EB systems. For the investigation of the reversal mechanisms via LTNO, Co/Au/CoO trilayers were chosen because of their large EB effects. The extremely thin CoO films (2 nm) consist of small grains [GR00a], and are dominated by one easy axis, induced by the initial applied magnetic field (cf. chapter 3).

According to SQUID magnetization curves (see Fig. 4.3 of chapter 4), observed for Co/CoO and Co/Au/CoO layers (see also Refs.[GR00b, GGR01]), cooled from above T_N in a positive field of 400 mT to 10 K, the first field cycle can be characterized by a sharp jump from positive to negative magnetization, while the return sweep shows a more rounded curve at the magnetization reversal. The occurrence of this asymmetry resembles a simple one-dimensional model [MSBK87], in which the sharp magnetization reversal (from positive to negative magnetization) may be interpreted as being related to domain wall motion, as opposed to the reversal from negative to positive magnetization, where at least parts of the magnetization are rotated, leading to more rounded hysteresis loops.

By monitoring the counting-rate ratio of the two γ-ray detectors, D1 and D2, the measurements may be used to distinguish between reversal processes dominated by domain wall motion as opposed to rotation of the magnetization. The data indicate an asymmetry (in the ratio) of the γ-ray intensities as the magnetic field is swept through the hysteresis curve (see Fig. 6.11) for both the ^{60}Co and ^{198}Au radioactive probes, but (as expected), not for the ^{54}Mn in Ag. The flatter response across the magnetization reversal (left-hand peak structures for Co and Au probes in Fig. 6.11 and Fig. 6.12) can be interpreted as being dominated by a breakup into domains with parallel or antiparallel orientation with respect to the applied field and showing less spin rotation. The higher ratio on the return sweep (right-hand peak structures in Fig. 6.11 and Fig. 6.12) is consistent with a magnetization reversal process that is dominated by domain rotation. It should be noted that a square hysteresis response would be observed in the simple case where the sample contains only domains oriented parallel or antiparallel to the applied field.

In summary, the LTNO method has the potential to investigate magnetization reversal processes, as has been demonstrated by observing the magnetic moments in the FM layers and the induced magnetic nuclear moments in the Au spacers at the same time.

6.6 Conclusions and summary of the LTNO results

The experimental finding of nuclear alignment of non-magnetic spacer atoms at the interfaces adjacent to magnetic FM and AFM layers is closely related to magnetic interlayer coupling. This has been demonstrated in earlier studies for several FM/spacer/FM systems [RDF$^+$97], [KNES94], [Pha02].

In these investigations, nuclear alignment in non-magnetic spacers was ob-

served to be mainly restricted to the interfacial spacer atoms. The latter was confirmed for the present experiments on AFM/spacer/AFM and FM/-spacer/AFM EB systems, using FM Co, AFM CoO and Au spacer layers. The experiments reveal that at least the Au interfaces are polarized at both types of interfaces (FM/Au and AFM/Au).

The experiments on Co/Au/CoO EB trilayers also revealed that the Au nuclear moments follow the Co moments during the magnetization reversal processes. In the EB state, the EB effect could be observed simultaneously for the Co and the interfacial Au nuclear moments in different samples with increasing Au spacer thicknesses.

This result may indicate the existence of an interlayer coupling between FM and AFM across a non-magnetic spacer, where at least the interfacial spacer atoms play an active role.

The potential of LTNO to investigate magnetization reversal processes in a degree of detail not obtained from conventional magnetometry methods has been demonstrated. The LTNO method is sensitive to observation of the magnetization reversal process through the induced magnetism in the interfacial Au atoms located between the FM (Co) and the AFM (CoO) layers. The present results correspond to asymmetric magnetization reversal processes on opposite sides of the hysteresis loop. This asymmetry appears as height asymmetry of the peak intensities during the magnetization reversal processes. The reversal process at decreasing fields opposite to the initial magnetization field seems to be dominated by a break-up into domains pointing either parallel or antiparallel to the applied field, while the reversal process on the opposite side of the hysteresis loop, i.e. at increasing fields, is dominated by magnetization rotation. This result confirms those obtained via polarized neutron reflectometry on a [Co/CoO/Au] multilayer consisting of individual Co/CoO bilayers (see chapter 5).

The experiment on a simple Co/Au/Co trilayer confirms that very thin Au films on Co are likely not to be continuous. Thus the presence of pinholes is expected for thin Au spacers of 0.5 nm thickness. The measurement on a Co/Au/Co trilayer revealed the hyperfine field value for the interfacial Au (78.3 T) to approach the value found for Au as an impurity in Co (87.03 T) in earlier studies [EEH+86]. As to be expected, the nuclear alignment of Co and Au at the Co/Au interface have proved to be collinear in this system.

The experiments on CoO/Au/CoO are the first investigations of AFM-/spacer interfaces with sensitivity to the interfacial nuclear alignment in the spacer. Within experimental accuracy, no average alignment of Co moments in the CoO layer was detected. This could be due to magnetically non-aligned CoO grains and/or to very long nuclear spin relaxation times for Co in this system. However at least the interfacial CoO must have been partially aligned,

since the interfacial Au at the CoO interface was polarized, and the angle between the axis of its nuclear alignment and the applied field was found to be $\Theta = \pm 62°$ for a 0.5 nm Au spacer. Furthermore, a drastic reorientation of the Au nuclear alignment took place upon increasing the spacer thickness. Hence the Au interface can be used as a sensor to probe the interfacial CoO layer.

At this stage it is difficult to draw conclusions about magnetic coupling between two CoO layers, since for this purpose, a change in orientation between two different CoO layers would have to be detected separately in the layers. (This could possibly be more readily observed using FM sensor layers outside each of the CoO films).

However, it can be concluded from this result that the AFM CoO causes a canting of the interfacial Au spins. In comparison to the large canting angle observed for CoO/Au/CoO trilayers, the interfacial Au moments in the Co/Au/CoO EB system were found to be canted at a smaller angle of about 21° with respect to the applied field. Since Co and Au were observed to be aligned in a simple Co/Au/Co layer, the canting in the EB systems is expected to be induced mainly at the AFM CoO interface, which must be partially aligned. The angle appears to be smaller because it is determined from the average alignment of two different interfaces. The alignment of the nuclear Au moments at the CoO/Au interfaces is expected to originate from uncompensated spins at the CoO interface, giving rise to a net interface magnetization. The existence of uncompensated spins in the CoO layer in a comparable Co/CoO EB bilayer has been experimentally confirmed by M. Gruyters *et al.* [GR00b]. Approximately 50% of the CoO interface has been found to be uncompensated in this particular system. Uncompensated interfacial spins have also been seen in CoO/MgO multilayers with much thicker CoO layers (10 nm - 300 nm) by Takano *et al.* [TKB+97]. The interfacial uncompensated moments, for their part, may interact with an external field or/and with an adjacent FM layer. They may further act as possible pinning centers for AFM domain walls forming upon cooling an AFM with uncompensated spins below the blocking temperature, even in zero field. The presence of uncompensated spins at FM/AFM interfaces in granular EB systems was theoretically addressed by the model proposed by Stiles and McMichael [SM99b]. This model suggests that the coupling at the FM/AFM interface is determined by two different contributions: a) direct coupling of the FM to the net moment of the AFM interface, which accounts for the undirectional shift, and b) the formation of partial domain walls in the AFM upon rotation of the FM magnetization, reducing the interfacial energy. The model implies that the net magnetization of the AFM interface and the magnetization of the FM layer are not necessarily collinear, due to the pinning of the uncompensated spins to the (bulk) AFM.

In summary, in the present work it was shown that LTNO is well suited

to study the induced spin polarisation at the interfaces in Co/Au/CoO EB systems and related systems. The EB effect was observed in the interfacial Au, where the nuclear Au moments seem to simply follow the nuclear Co moments during the magnetization reversals. In magnetic saturation at 500 mT, the Au moments were canted away at an angle Θ_{Au} from the Co moments and from the applied field axis. The canting was found to occur at the CoO/Au interface, since investigations on a simple Co/Au/Co trilayer revealed collinear alignment at the Co/Au interfaces. In contrast, measurements on CoO/Au/CoO trilayers have shown that the axis of nuclear alignment of the Au is strongly canted away from the applied field axis. Nuclear alignment of the Au moments at a CoO/Au interface implies that the interfacial CoO is at least partially magnetically aligned.

Outlook

In any case, the observation of a canting angle Θ_{Au} at the CoO/Au interface imposes the question as to whether the interfacial magnetic moments at the Co/CoO interface in a simple bilayer would also show non-collinear alignment.

For the present systems this cannot be measured with LTNO, since the ^{60}Co signals emitted from the Co and CoO layers cannot be separated. One possibility to get information about a Co/CoO interface via LTNO is to produce samples with even thinner Au layers, using ^{198}Au sensor atoms to probe the relative alignment at the interface. An important goal for the future would be to investigate the interfacial alignment in Co/Au/CoO systems with very thin Au spacer layers, focusing on the angle between the average Au nuclear alignment and the Co magnetization with decreasing Au thickness. It would be interesting to know how the average canting angle Θ_{Au} of the Au moments in a Co/Au/CoO trilayer changes upon reducing the Au spacer thickness. If the angle Θ_{Au} does not decrease with decreasing Au spacer thickness, one could conclude that the interfacial moments in Co and CoO in a simple bilayer are noncollinear. If on the other hand Θ_{Au} decreases with decreasing Au spacer thickness, this would strongly indicate collinear alignment of the magnetic moments at the interface. This would further suggest that the interfacial moments in a CoO interface tend to relax to an angle Θ_{CoO} upon introducing a spacer which separates the CoO interface from the Co interface.

In addition, the non-magnetic Au probes could be replaced by Ag, or the FM Co layer could be replaced by Fe, Ni or other FM materials in order to obtain direct information about FM/CoO interfaces. Other AFM materials could be used as well, e.g. the transition metal oxides FeO and NiO. Similar experiments as those presented in this work on layer systems with related magnetic properties, such as those proposed above, could be performed and

compared with the present results. However, when selecting the magnetic and non-magnetic components of such a layer system, one has to take care that at least one of the selected components provides a suitable radioactive probe isotope upon irradiation.

To obtain more detailed quantitative results for the precise behavior of the magnetic moments of FM and non-magnetic spacer atoms during the reversal processes, improved statistics are required. Therefore further investigations on similar and related systems will have to be performed.